

# Repeated syn- and post-orogenic gold mineralization events between 1.92 and 1.76 Ga along the Kiistala Shear Zone in the Central Lapland Greenstone Belt, northern Finland



Ferenc Molnár<sup>a,\*</sup>, Alexander Middleton<sup>a,1</sup>, Holly Stein<sup>b,c</sup>, Hugh O'Brien<sup>a</sup>, Yann Lahaye<sup>a</sup>, Hannu Huhma<sup>a</sup>, Lassi Pakkanen<sup>a</sup>, Bo Johanson<sup>a</sup>

<sup>a</sup> Geological Survey of Finland, P.O. Box 96, Espoo FI-02151, Finland

<sup>b</sup> AIRIE Program, Campus Mail 1482, Colorado State University, Fort Collins, CO 80523-1482, USA

<sup>c</sup> Centre for Earth Evolution and Dynamics (CEED), P.O. Box 1028, University of Oslo, 0315 Oslo, Norway

## ARTICLE INFO

### Keywords:

U-Pb geochronology  
Disturbed Re-Os system in arsenopyrite  
Pb-isotopes in galena  
Hydrothermal monazite and xenotime, orogenic gold  
Central Lapland Greenstone Belt  
Svecofennian Orogeny

## ABSTRACT

The Central Lapland Greenstone Belt (CLGB) is well endowed with orogenic gold deposits along major shear zones and structural lineaments. In the northern part of the belt, the Kiistala Shear Zone (KISZ) hosts the Suurikuusikko gold deposit (Kittilä Mine), currently the largest gold producer in Europe. The Iso-Kuotko deposit is located 10 km to the north of Suurikuusikko along the same shear zone. Gold mineralization at Iso-Kuotko formed in two major stages: an early stage refractory gold mineralization with auriferous arsenopyrite with similarities to the ore at Suurikuusikko and a late, main stage mineralization with free gold in carbonate-quartz veins with abundant pyrrhotite, native bismuth and other sulphide minerals. This latter ore is absent at Suurikuusikko. Based on U-Pb dating, as well as Re-Os and Pb-isotope systematics of rock-forming and hydrothermal minerals, we evaluate the relationships between tectonic evolution and formation of gold deposits throughout the late Palaeoproterozoic in the northern part of the CLGB.

Results from *in situ* U-Pb dating of zircon and petrographically well constrained hydrothermal monazite and xenotime by LA-ICPMS, and model age calculations using Re-Os isotopic data for arsenopyrite and *in situ* Pb-isotope data for galena from the Iso-Kuotko deposit provide evidence for multiple episodes of hydrothermal activity along the KISZ. Data suggest coincident felsic magmatism and structurally controlled fluid flow events during wrench fault-dominated N-S shearing associated with early, micro-continent accretion ushering in the Svecofennian orogeny. This includes the formation of refractory gold ores at Suurikuusikko ( $1916 \pm 19$  Ma) and Iso-Kuotko ( $> 1868 \pm 15$  Ma). Subordinate barren veining took place at  $\sim 1830$  Ma during transient extension between the accretion and final collision stage. Xenotime in late stage veins with visible gold at Iso-Kuotko yield U-Pb ages between  $1761 \pm 9$  and  $1770 \pm 7$  Ma. This time-interval is concurrent with widespread granitoid emplacement at the close of the Svecofennian orogeny. Disturbance of the Re-Os system in the early auriferous arsenopyrite can be connected to the late stage mineralizing processes. Pb isotope data suggest a mixed mantle and lower crust origin for fluids in the post-orogenic hydrothermal system.

*In situ* U-Pb dating in polished thin sections in tandem with electron microprobe analyses of mineral compositions and detailed textural observations, highlights the utility of xenotime and monazite as robust geochronometers capable of recording repeated hydrothermal events in Paleoproterozoic orogenic systems. Results provide precise temporal constraints for orogenic gold mineralization and vital information to refine the tectonic evolution of the Central Lapland Greenstone Belt.

## 1. Introduction

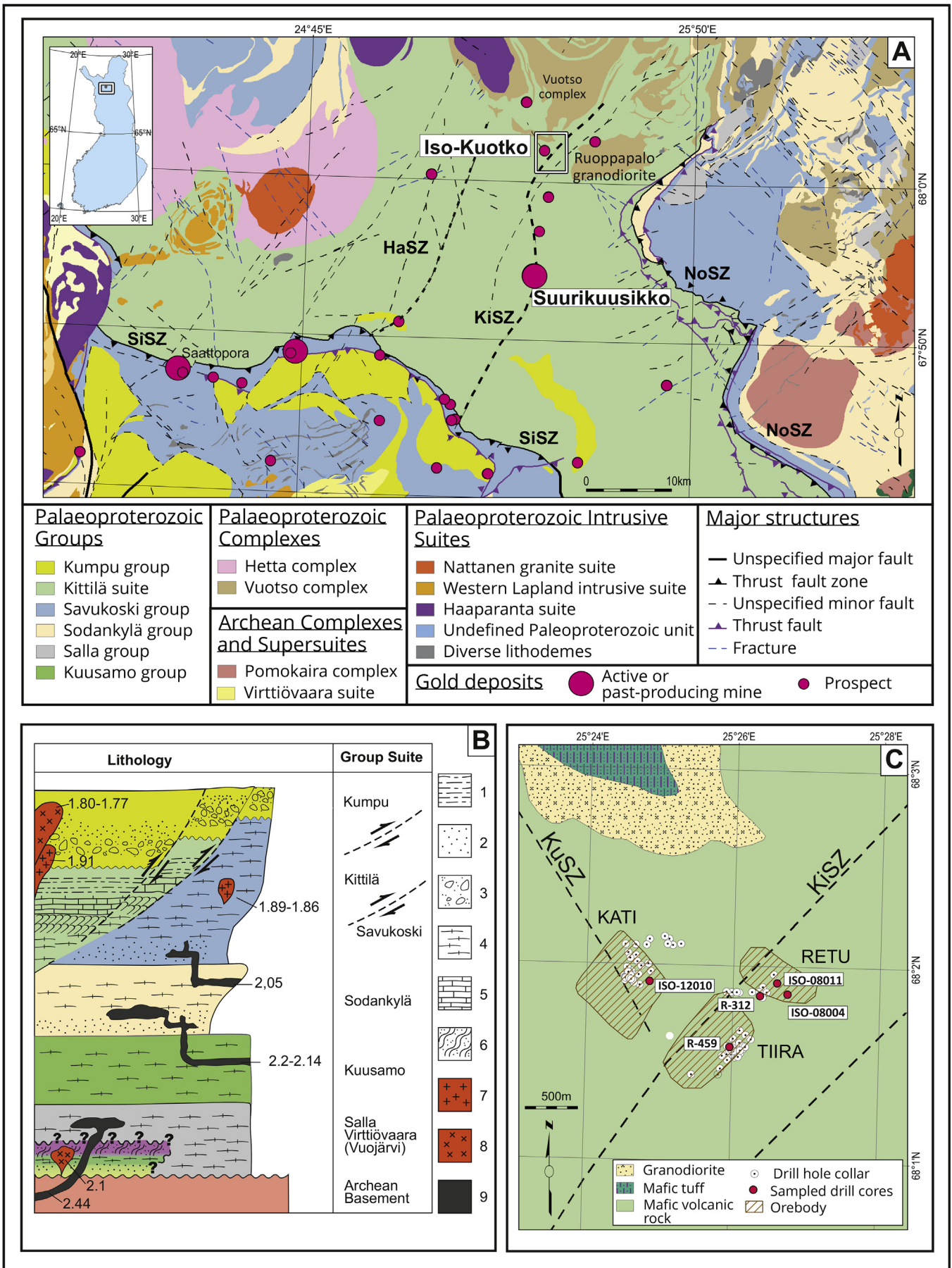
The temporal relationship between the formation of orogenic gold

deposits and the major structural, magmatic and metamorphic events is a crucial parameter to understand metallogeny of orogenic belts and establishing geological models applicable to mineral exploration

\* Corresponding author.

E-mail address: [ferenc.molnar@gtk.fi](mailto:ferenc.molnar@gtk.fi) (F. Molnár).

<sup>1</sup> Present address: Gerald UK Ltd., Grand Buildings Trafalgar Square, London WC2N 5HR, United Kingdom.



(caption on next page)

**Fig. 1.** Regional geology and stratigraphy of the Central Lapland Greenstone Belt and local geology at the Iso-Kuotko gold deposit. A – regional geology of the CLGB with locations of major orogenic gold deposits and showings, and major structures (simplified from the DigiKP electronic map database of the Geological Survey of Finland). KiSZ – Kiistala Shear Zone; SiSZ – Sirkka Shear Zone; NoSZ – Nolppio Shear Zone; HaSZ, Hanhima Shear Zone. B – stratigraphy in the CLGB (according to Hanski and Huhma, 2005; Lahtinen et al., 2015a); 1 – metasedimentary-clastic metavolcanic rocks, undivided; 2 – quartzite; 3 – conglomerate; 4 – felsic and mafic volcanic rocks, undivided; 5 – graphitic schist; 6 – gneiss; 7–8 – granitoid intrusions of different ages; 9 – mafic sills and dikes of different ages. C – local geology at the Iso-Kuotko gold deposit (modified after Eilu et al., 2007) with the major orebodies and location of drillcores sampled in this study shown. KuSZ – Kuotko Shear Zone.

(Groves et al., 2003; Goldfarb et al., 2005; Robert et al., 2005; McCuaig et al., 2010; Groves and Santosh, 2016). Distinction of regional and local ore forming and barren hydrothermal events during the complex and elongated structural evolution of accretional and collisional belts, as well as during the re-activation of old structures in old cratonic areas by overprinting orogenies requires application of robust geochronological methods with strict structural and textural context of minerals applied to age dating (Vielreicher et al., 2002, Carpenter et al., 2005; Zhang et al., 2014; Vielreicher et al., 2015; Gazley et al., 2016; Molnár et al., 2016; Molnár et al., 2017; Fourgerouse et al., 2017; Fielding et al., 2017).

The Central Lapland Greenstone Belt (CLGB) in northern Finland (Fig. 1) was deformed and metamorphosed during the prolonged, 1.92–1.77 Ga Svecofennian orogeny. The CLGB hosts numerous orogenic gold deposits, which are mostly located along the major Kiistala and Sirkka Shear zones (KiSZ and SiSZ, respectively), including the economically superior Suurikuusikko deposit and the small Iso-Kuotko deposit just a few kilometres to the north from Suurikuusikko along the KiSZ (Fig. 1A). Although there are some similarities, these deposits also show significant differences, especially in the texture of ore and mode of gold enrichment. The refractory gold content of Suurikuusikko ore is hosted within the crystal structure of pyrite and arsenopyrite, which are disseminated in hydrothermally altered rocks and veins (Wyche et al., 2015), whereas the gold mineralization hosted by veins at Iso-Kuotko is characterized by the occurrence of free gold grains with subordinate amounts of refractory gold (Härkönen et al., 2000). In this study, we address the contemporaneity of large-scale hydrothermal systems and the superimposition of temporally distinct hydrothermal events along the KiSZ.

Rare-earth element-rich phosphate minerals, xenotime and monazite, are ideal for precise geochronology due to their relatively high U and low Pb concentrations, resistance to metamictisation, high “closure” temperatures (> 700 °C for xenotime and > 500 °C for monazite; Cherniak, 2006; Cherniak et al., 2004; Kositcin et al., 2003; Seydoux-Guillaume et al., 2012) and their ability to crystallise over a range of temperatures in different geological environments (Hetherington et al., 2008; Rasmussen et al., 2011; Vallini et al., 2002, 2005; Vielreicher et al., 2015). However, as these two phosphates are also susceptible to alteration (Gysi et al., 2015; Harlov and Wirth, 2012; Hetherington and Harlov, 2008; Hetherington et al., 2010; Poitras et al., 2000; Seydoux-Guillaume et al., 2012; Williams et al., 2001), meticulous petrographic and mineral-paragenetic studies should be completed before using these minerals for chronological work.

Here we present precise U–Pb ages for hydrothermal xenotime and monazite from the Iso-Kuotko deposit using *in situ* laser ablation inductively coupled mass spectrometry (LA-ICPMS). The U–Pb ages are compared with Re–Os analyses of arsenopyrite. This paper also presents the results of *in situ* Pb-isotope analyses of galena and U–Pb dating of rock forming zircon from the Suurikuusikko and Iso Kuotko deposits. The new data together with the results from previous geochronological studies are used to evaluate relationships between regional tectonic evolution and the formation of gold deposits throughout the late Palaeoproterozoic in the northern part of the CLGB.

## 2. Geological setting

### 2.1. Regional geology

The CLGB of northern Finland is exposed over an area of ~100 by 200 km (Fig. 1A) and is a part of one of the largest known Paleoproterozoic greenstone belts, which extends from northern Norway to Russian Karelia (Hanski and Huhma, 2005). The CLGB is an emerging mining district. Modern exploration in this region started in the mid 1980s and resulted in discoveries of more than 60 orogenic gold deposits and occurrences. Of these, only the Suurikuusikko deposit is currently being mined, but this deposit is presently the largest primary gold producer in Europe (Kittilä Mine, 177,374 oz Au production in 2015; Agnico-Eagle, 2015). Exploration is still active along the KiSZ, the major structure in the northern part of the CLGB controlling the location of the Suurikuusikko deposit and several other gold occurrences. One of those projects targets the area of the Iso-Kuotko deposit, which is located about 12 km to the north of the Kittilä Mine, along the intersecting zone of the of the KiSZ and other NE–SW and NW–SE trending shear zones (Fig. 1).

The supracrustal evolution of the CLGB lasted for several hundred million years, from the early Paleoproterozoic (~2.44 Ga) intracontinental rifting of the Archaean (Karelian) basement through prolonged basin evolution with predominant deposition of extensive sedimentary and volcanic sequences until the termination of the basin evolution by the Svecofennian orogeny at around 1.92 Ga (Korja et al., 2006; Lahtinen et al., 2005). The Salla Group contains the lowermost units of the CLGB and unconformably overlies Archaean basement gneiss of c.3.0–2.6 Ga age (Hanski and Huhma, 2005; Fig. 1B). It is composed of ~2 km of felsic to intermediate volcanic sequences intruded by mafic–ultramafic layered intrusions. The early Palaeoproterozoic, 2440 Ma age of this group is constrained by U–Pb zircon ages of layered intrusions (Mutanen and Huhma, 2001). Along the southern margin of the CLGB, quartzite, mica gneiss and felsic to intermediate volcanic rocks of the Vuojärvi Group appears to form a transitional unit between the Archaean basement and the volcanic sequence of the Salla Group (Eilu and Niiranen, 2013). The Salla Group is overlain by the tholeiitic to komatiitic metavolcanic rocks of the Kuusamo (previously Onkamo) Group of 2.44–2.20 Ga age (Lehtonen et al., 1998; Hanski and Huhma, 2005). Volcanic activity partially ceased during successive deposition of the Sodankylä Group in a widening rift basin. Group stratigraphy consists of tidal derived quartzites, mica schists, minor stromatolitic carbonates and mafic metavolcanic rocks. Minimum age estimates for Sodankylä Group metasediments are provided by the occurrence of c.2.20 Ga cross-cutting differentiated mafic–ultramafic sills (Hanski and Huhma, 2005). The overlying Savukoski Group accumulated in a deepening sedimentary basin environment as seen from the occurrences of phyllitic and black, graphite-/sulphide-bearing schistose metasediments intercalated with minor mafic tuffites (Lehtonen et al., 1998). These are overlain by volcanic rocks with komatiitic and picritic chemical affinities. A minimum age of 2.05 Ga for the pelitic metasedimentary rocks (Hanski and Huhma, 2005) is provided by the U–Pb zircon age for the intruding layered mafic intrusions (Mutanen and Huhma, 2001). The Savukoski Group is overlain by the obducted and allochthonous Kittilä Group, which represents one of the largest

accumulations ( $> 2600 \text{ km}^2$ ; Hanski and Huhma, 2005) of mafic volcanic rock sequences in Fennoscandia. It is 6–9 km thick and consists of Fe- to Mg-tholeiitic basalts, plagioclase porphyry felsic intrusions, banded iron formations and metasedimentary packages including metagreywackes, phyllites and graphite- to sulphide-bearing schists. U–Pb zircon crystallization ages put emplacement of felsic intrusions at c.2.01 Ga (Rastas et al., 2001; Hanski and Huhma, 2005), contemporaneous with basaltic volcanism (Lehtonen et al., 1998). The Kittilä Group is then unconformably overlain by the Kumpu Group, which is the uppermost unit of the CLGB. The molasse-like Kumpu Group comprises thick sedimentary packages of metamorphosed sandstones, polymict conglomerates and siltstones. Detrital zircon studies of granitic conglomerate clasts from this unit indicate deposition likely occurred post-1880 Ma (Hanski and Huhma, 2005). Ward et al. (1988) suggested that the Kumpu Group rocks represent late-stage synorogenic sedimentation in small strike-slip basins.

The Paleoproterozoic rock units in the CLGB have undergone several stages of deformation and metamorphism during the Svecofennian orogeny. The  $D_1$  to  $D_4$  stages of deformation spanned approximately between 1.92 and 1.77 Ga (Lahtinen et al., 2005; Patison, 2007; Eilu and Niiranen, 2013). However, temporal constraints of the deformation stages are indirectly determined, mostly by cross-cutting relationships of faults with dated granitic rocks and displacements of early thrust structures by later ones. The main  $D_1$  and  $D_2$  ductile deformation stages are attributed to the predominantly East and North directed compression and thrusting between c.1.93 and 1.91 Ga (Daly et al., 2001; Hölttä et al., 2007; Lehtonen et al., 1998; Niiranen et al., 2014; Patison, 2007; Saalman and Niiranen, 2010; Tuisku and Huhma, 2006). The first stage of the Svecofennian micro-continent accretion at around 1.92 Ga in the northern part of Fennoscandia generated east-vergent thrusting of the Kittilä Group over and under the Savukoski Group along the SE–NW and NE–SW trending Nolppio Shear Zone (NoSZ), which has variable dips to the northeast and southwest, respectively, in the north-eastern and eastern part of the CLGB (Fig. 1A; Rastas et al., 2001; Hanski and Huhma, 2005; Hölttä et al., 2007; Lahtinen et al., 2005; Nironen, 2017). Compression from the west and east resulted in development of large-scale folding with a N–S axial plane and a wavelength of 6–10 km ( $D_1$  deformation). Change of orientation of thrusting from E–W to N–S led to a superimposed folding ( $D_2$  deformation) at around 1.92–1.91 Ga. In the southern part of the CLGB, the thrust of the Kittilä Group under the Savukoski Group is marked by a southwest-dipping, ESE–WNW running SiSZ (Fig. 1A; Gaál et al., 1989; Hölttä et al., 2007; Niiranen et al., 2014). During 1.91–1.88 Ga the direction of thrust rotated between NW–SE and NE–SW and the  $D_3$  deformation stage can be related to this variation of stress field (Ward et al., 1988; Patison, 2007). The NW–SE compression in the central part of the CLGB resulted in crenulation folding with NE-striking axial plane (Nironen, 2017). Oblique slip between the major deformation fronts generated numerous NNE–SSW striking shear zones by reactivation of transfer faults (Ward et al., 1988), among which the KiSZ hosts the Suurikuusiikko gold and Iso-Kuotko gold deposits and several other small occurrences of gold mineralization (Fig. 1A). However, studies by Patison (2007) concluded that repeated movement took place within the KiSZ and the early sinistral strike slip faulting was followed by dextral movement during the rotation of maximum principal stress. Intense re-activation of the E–W oriented SiSZ under NE–SW oriented compression was also recognized and some of these re-activation events can be as young as 1.85–1.80 Ga (Patison, 2007; Niiranen et al., 2014; Nironen, 2017). The  $D_4$  brittle deformation is widespread but the related N–S and NW–SE oriented fracture systems are discontinuous and may have resulted from relaxation-related extension concomitant with 1.79–1.76 Ga post-orogenic granite emplacement in a belt extending from the western part of the CLGB to Murmansk, Russia (Nironen, 2005; Patison, 2007).

The central part of the CLGB is dominated by tholeiitic basalts of the Kittilä Group (Fig. 1A) at greenschist facies metamorphic grade. A

regional high and low pressure mid-amphibolite facies belt bounds this area on the north whereas the gradual increase of metamorphic grade from greenschist to amphibolite facies on the west and south is related to the Western Lapland and Central Lapland granitoid plutons (Hölttä et al., 2007). The age of metamorphism in the CLGB is not well constrained but it is generally accepted that the peak metamorphic conditions were reached between 1.88 and 1.86 Ga (Lahtinen et al., 2015a).

Precise radiometric ages for formation of orogenic gold deposits in the CLGB are limited. Previous U–Pb and Pb–Pb geochronological studies used zircon, titanite, rutile, monazite, galena and other sulphide mineral separates from the host rocks and vein fillings with little textural control on relationships to stages of gold deposition. Despite this, previous studies bracket formation of orogenic Au deposits into two periods, 1.92–1.88 and 1.85–1.78 Ga (Mänttari, 1995; Patison, 2007; Lahtinen, 2012; Eilu, 2015), corresponding to the (microcontinental) accretion and continent–continent collision stages, respectively, during the Svecofennian tectonic evolution (Lahtinen et al., 2005; Korja et al., 2006). Re–Os isochron dating of arsenopyrite, the major carrier of refractory gold, constrained a  $1916 \pm 16 \text{ Ma}$  age for the mineralization at Suurikuusiikko (Wyche et al., 2015); this age is indistinguishable from the ages of felsic porphyry dikes and intrusions occurring in the vicinity of the deposit. Rastas et al. (2001) reported  $1919 \pm 8 \text{ Ma}$  for the Nyssäkoski porphyry dike ( $\sim 10 \text{ km}$  southwest of Suurikuusiikko). These intrusive rocks are weakly to strongly foliated suggesting their Svecofennian syn-orogenic origin (Hanski and Huhma, 2005; Rastas et al., 2001).

## 2.2. Deposit geology

The Iso-Kuotko gold deposit ( $68^\circ 15' \text{N}$ ,  $25^\circ 25' \text{E}$ ) is located approximately 70 km northeast of the town of Kittilä and 12 km north of the Suurikuusiikko gold deposit, where the NE-trending KiSZ connects with oblique, NW-striking splay faults of the Kuotko Shear Zone (KuSZ) (Fig. 1A and C; Härkönen et al., 2000). Slip lineation measurements indicate oblique dextral movement with a shallow plunge (SE–SW; Patison, 2000). The KuSZ displaces  $D_1$ – $D_2$  structures further to the NW, thus the inferred age of this structure is also  $D_3$  (Patison, 2007).

The host rocks of the mineralization belong to the Kittilä Group and consist of greenschist facies tholeiitic basalt lava flows with intercalated tuffs and felsic porphyry dikes with highly variable thicknesses (Fig. 1C and 2). Locally, lamprophyre dikes also cut the volcanic units. Mänttari (1998) obtained a  $1915 \pm 55 \text{ Ma}$  (MSWD = 160) U–Pb zircon crystallization age from one of the felsic porphyry dikes in the Kati orebody and reported a  $1718 \pm 9 \text{ Ma}$  (MSWD = 19) Rb–Sr isochron age using separated biotite and apatite, as well as whole rock samples from the lamprophyre dikes. Granitoid rocks of the Paleoproterozoic Vuotso complex also intrude the mafic volcanic sequence in the vicinity of the mineralization (Fig. 1A and C). The Ruoppapalo pluton ( $1914 \pm 3 \text{ Ma}$  and  $1905 \pm 5 \text{ Ma}$ ; Rastas et al., 2001; Ahtonen et al., 2007, respectively), a part of the Vuotso Complex, outcrops  $\sim 3 \text{ km}$  to the east of the Iso-Kuotko deposit (Fig. 1A) and is heterogeneous with typically coarse-grained granitic–quartz dioritic–tonalitic compositions. The volcanic rocks up to 1–3 km away from the intrusion contact are metamorphosed to amphibolite grade, whereas those peripheral to this zone experienced greenschist facies metamorphism (Hölttä et al., 2007).

The Iso-Kuotko mineralization is composed of 3 principal orebodies a few hundred meters apart (Fig. 1C): Kati, Tiira and Retu (including the small Nimetön orebody). The Tiira and Retu orebodies are located along the NE-trending KiSZ whereas Kati forms a mineralized zone along the KuSZ. These orebodies consist of auriferous quartz–carbonate–sulphide veins and breccias. According to Härkönen et al. (2000), the host rocks show carbonatization, albitization and pyritization along the veins, but the width of the intensely altered zones is very narrow, less than ten centimetres. On the basis of Pb-isotope studies, Mänttari (1995) proposed two major stages of ore deposition: an early

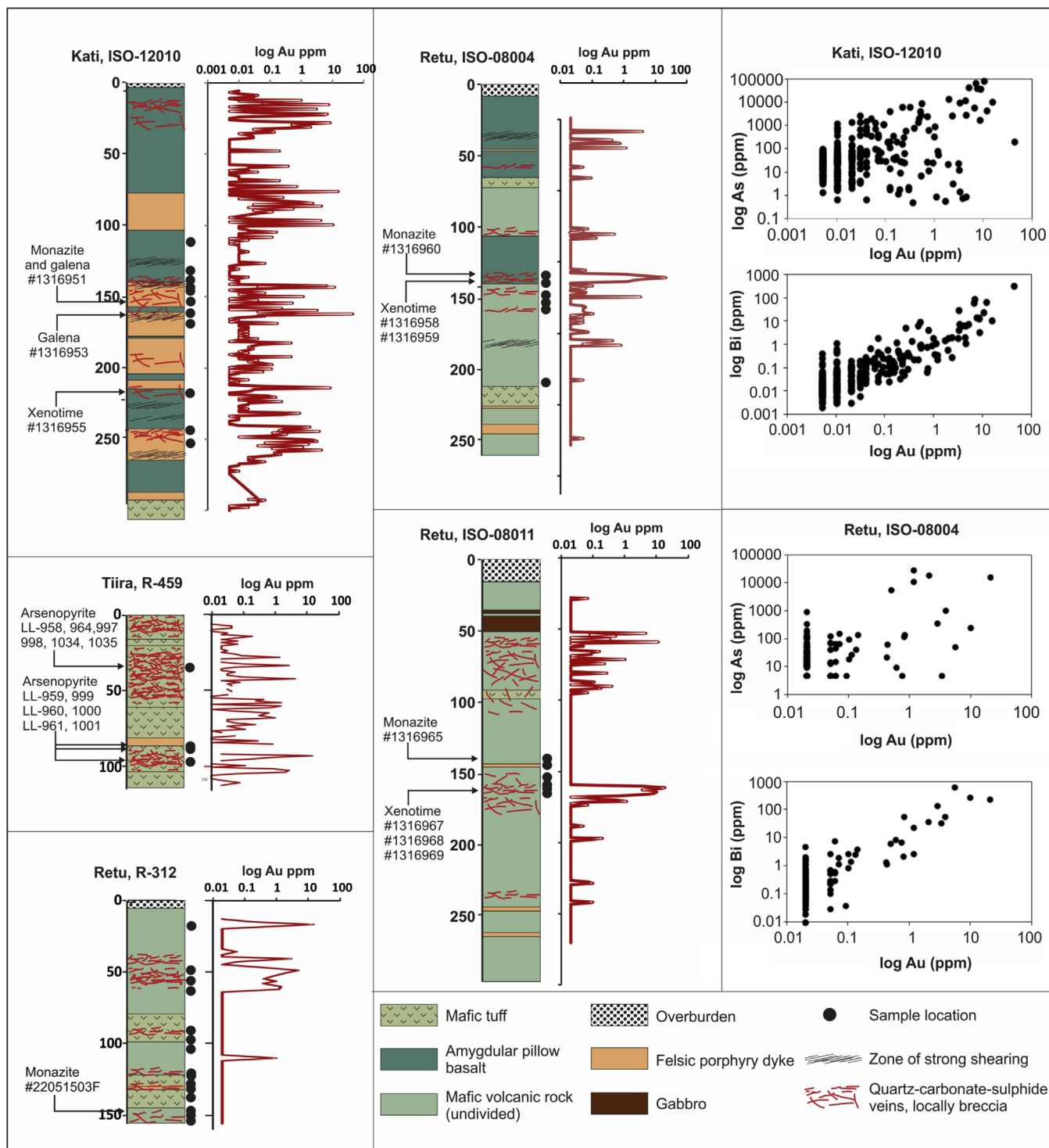


Fig. 2. Logs of drillholes showing gold concentrations, locations of samples collected for this study and correlation of gold concentrations with bismuth and arsenic for two of the sampled drillcores.

synorogenic sulphide and a late stage gold-sulphide mineralization. Regression of Pb-isotope data suggested  $1718 \pm 40$  Ma for the latter hydrothermal event. Results of Pb-isotope model calculations by Manttari (1995) also indicated the possible effects of the Caledonian orogeny at 500–420 Ma on the Pb-isotope systems of sulphides. However, Härkönen et al. (2000) reported three phases of mineralization that are identical in all three orebodies at Iso-Kuotko. The first ore phase is composed of quartz + carbonate veins with pyrite + arsenopyrite + pyrrhotite ± chalcopyrite ± sphalerite ± galena hosted by

NW-SE trending shear zones dipping to NE at ~40–50. Native gold is a late mineral in these veins as it occurs in cracks of sulphides. The second mineralization phase is confined to sub-vertical quartz + carbonate-dominated vein system with a similar NW strike. These veins are sulphide poor (galena + chalcopyrite) with native Au and Bi (± maldonite). The third purported phase of mineralization is represented by vertical N–S trending quartz veins, which also contain native gold grains with minor amounts of sulphide minerals. In contrast with results of other studies, Patison (2000) reported quartz-carbonate-

sulphide veins parallel with the NE, N and ENE striking shear zones. Patison (2007) also suggested that the deposit formed by a single mineralization event in conjunction with the D<sub>3</sub> stage of regional deformation in the CLGB on the basis of sinistral displacement of D<sub>1</sub>/D<sub>2</sub> thrusts and the undeformed nature of ore veins–breccias.

According to the results of preliminary metallurgical tests, gold occurs predominantly (80%) as free native grains, whereas the remaining is refractory within arsenopyrite and pyrite (Härkönen et al., 2000). Historical resource estimates are 170,000 t at 4.3 g/t Au and 121,000 t at 2.7 g/t Au for the Kati and Tiira orebodies, respectively (Härkönen et al., 2000). Since late 20th-century little exploration work was undertaken at Iso-Kuotko until recently. It is now owned and being explored by Agnico-Eagle Ltd, which estimates the current cumulative resources of the Iso-Kuotko deposit at 1.8 Mt with 2.89 g/t average Au content (Agnico Eagle, 2015).

### 3. Study methods

As the mineralization at Iso-Kuotko is largely covered by up to several meters thick Quaternary till sediments, samples representing different types of host rocks, barren and mineralized zones were exclusively collected from cores of exploration drill holes (ISO 12010 drill hole from the Kati orebody; ISO 08004, ISO 08011 and R-312 drill holes from the Retu orebody and R-452 drill hole from the Tiira orebody; Figs. 1C and 2). The strategy of sampling was to obtain a representative set of rock and vein/breccia samples from mineralised and un-mineralised parts of drillcores for investigating the relative timing of vein/breccia formation in relation to the deformation features in the host rocks and to constrain the temporal relationships between mineral assemblages and phosphate accessory minerals used for U–Pb dating. Geochemical data obtained from the Agnico-Eagle Finland Ltd. (“ISO” drillholes) and extracted from the geochemical data base of the Geological Survey of Finland (“R” drillholes) were used to locate sites of sampling in high grade and barren drill core intercepts. The geochemical database used for this purpose contained the concentrations of Au, Ag, base- and semi-metals from 0.8 to 1 m long half-drill core samples. Aliquots were produced by acid leaching and analysed by ICPMS at ALS Minerals Finland and at the former Department of Geochemistry at the Geological Survey of Finland (currently Labtium Ltd.). For better definition of the upper age limit of mineralization and to investigate the potential relationship between emplacement of the felsic porphyry dikes and formation of the mineralization, a polished mount was also prepared from the zircon grains which had been previously separated and analysed by thermal ionisation mass spectrometry (TIMS) from a mineralized felsic porphyry dike in the Iso-Kuotko deposit by Mänttari (1998). Samples for Re–Os studies were collected from arsenopyrite-rich, high grade intercepts in the R-452 drill hole.

Petrography of host rock alteration and ore mineralization was performed by transmitted and reflected light polarizing microscopy and scanning electron microscopy. Monazite and xenotime were located in polished thin sections using a JEOL JSM5900LV scanning electron microscope (SEM) equipped with a dispersive X-ray spectrometer (EDS) and INCA Feature phase detection–classification software (Oxford Instruments Ltd). INCA Feature software performs automatic scans over a user-defined sample area and detects grains of interest using the back-scattered electron detector. Minerals were subsequently analysed and classified by chemistry and size using the EDS software in a single run. The morphological characteristics and internal texture of zircon grains were also studied by SEM-EDS. Following mineral identification and textural classification, grains were imaged with a high resolution JEOL TM JSM-7100F Field Emission SEM (FE-SEM) at the Finnish Geoscience Research Laboratories (SGL), Geological Survey of Finland, Espoo. Compositions of monazite and xenotime grains were then determined with electron probe microanalysis in wavelength dispersive mode (WDS) using a CAMECA SX100, also at the SGL. Operating conditions for xenotime and monazite analysis were an accelerating voltage of

20 kV and probe current of 100 nA with a defocused beam diameter of 5 µm. K<sub>α</sub>-lines were used for Ti, Mn, Fe, Ca, F, Cl, P and Si in monazite but K<sub>β</sub>-lines for Si in xenotime. Aluminium was only analysed for xenotime using K<sub>α</sub>-lines. L<sub>α</sub>-lines were measured for Y, La, Ce, Yb and Zr; L<sub>β</sub>-lines for Nd, Sm, Gd, Pr, Tb, Dy, Ho, Er and Hf, and M<sub>α</sub>-lines for Th, U and Pb. Counting times varied from 10 s to 240 s for optimal detection limits of rare earth elements (REE), Th, U and Pb. X-ray lines and background positions were selected to minimise interferences between elements during analysis. Minerals, pure metals and synthetic REE + Y phosphates were used as calibration standards. Matrix corrections were calculated using the PAP procedure (Pouchou and Pichoir, 1987).

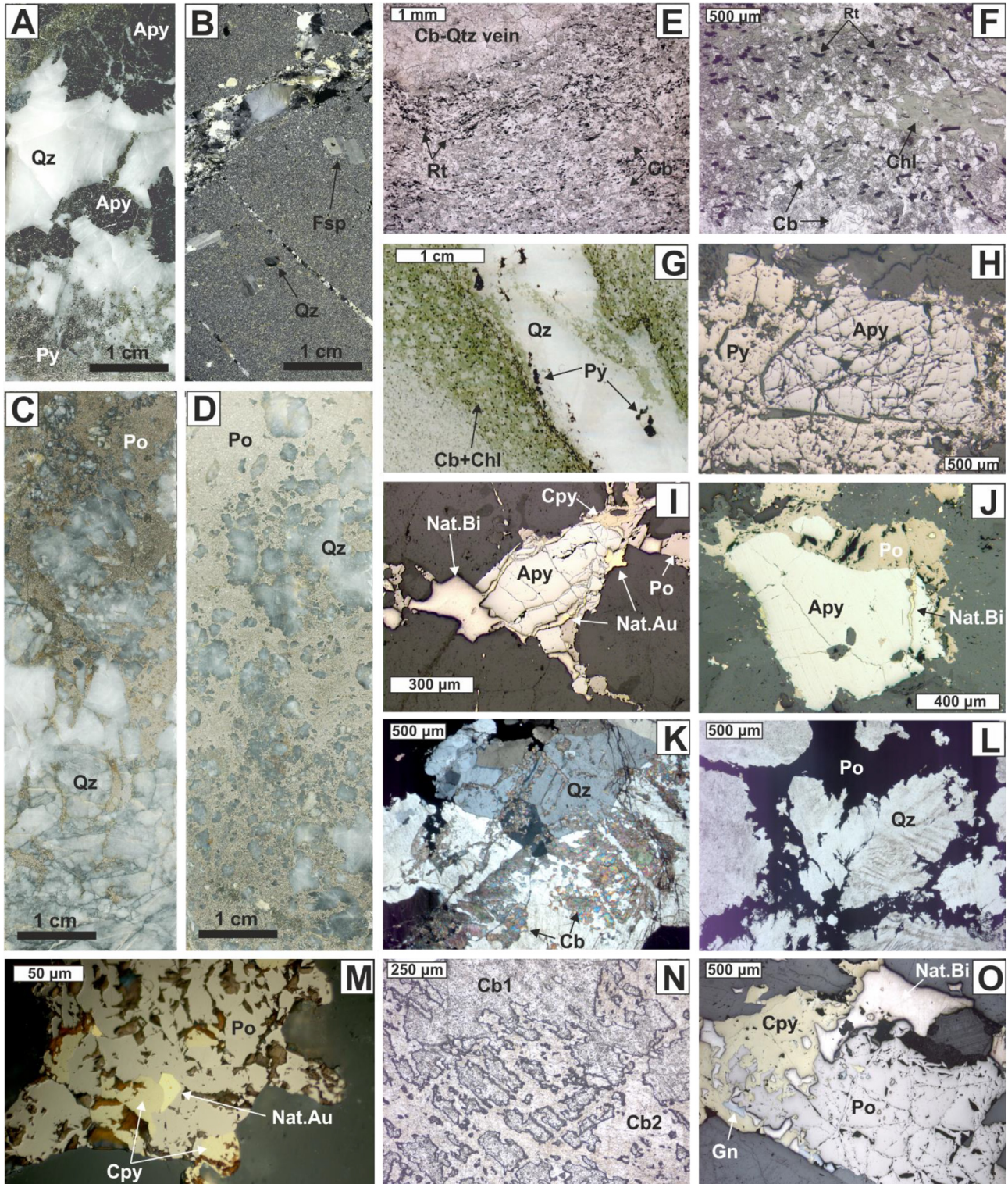
U–Pb dating of monazite and xenotime were performed using a Nu Instruments AttoM single collector ICPMS, connected to a Photon Machines Excite laser ablation (LA) system whereas U–Pb dating of zircon and Pb-isotope analyses of galena were performed by means of a Nu Plasma HR multicollector ICPMS connected to a Photon Machines Analyte G2 laser ablation (LA) system, both at the Finnish Geoscience Research Laboratories, Geological Survey of Finland, Espoo. Samples were ablated in He gas (gas flows = 0.4 and 0.1 l/min) within a HelEx ablation cell (Müller et al., 2009). The He aerosol was mixed with Ar (gas flow = 0.8 l/min) prior to entry into the plasma. The gas mixture was optimized daily for maximum sensitivity. All analyses were made in static ablation mode. Ablation conditions were: 25 µm beam diameter for zircon and monazite and 15 µm beam diameter for xenotime with 5 Hz pulse frequency and 0.55 J/cm<sup>2</sup> (zircon), 3 J/cm<sup>2</sup> (monazite) and 3.32 J/cm<sup>2</sup> (xenotime) beam energy density. A single U–Pb measurement included a short pre-ablation, 15 s pause for this material to be swept from the instrument, 20 s of on-mass background measurement, followed by 30–60 s of ablation. To minimize the effects of laser-induced elemental fractionation, the depth-to-diameter ratio of the ablation pit was kept low, and isotopically homogeneous segments of the time-resolved traces were calibrated against the corresponding time interval for each mass in the reference standard.

During analyses of xenotime and monazite by single collector ICPMS, masses 202, 204, 206, 207, 208, 232 and 238 were measured using a single secondary electron multiplier. <sup>235</sup>U was calculated from the signal at mass 238 using a natural <sup>238</sup>U/<sup>235</sup>U = 137.88. Mass number 204 was used as a monitor for common <sup>204</sup>Pb and mass 202 was monitored for Hg levels prior to and during ablation. In our ICP-MS system, <sup>204</sup>Hg almost exclusively originates from the He supply giving a background count rate on mass 204 of 200–300 cps (counts per seconds), which has been stable over the last several years. The contribution of <sup>204</sup>Hg from the plasma was eliminated by the on-mass background measurement. Signal strengths on mass 206 ranged from 10<sup>4</sup> to > 10<sup>6</sup> cps, depending on the uranium content and age of the minerals analyzed. In-house monazite standards A49 (1874 ± 3 Ma; TIMS) and A1326 (2635 ± 2 Ma; TIMS, Hölttä et al., 2000) and in-house xenotime standards A1298 (1852 ± 2 Ma; TIMS; Pajunen and Poutiainen, 1999) and A1244 (2616 ± 3 Ma; TIMS) were used for calibration. The calculations were done off-line, using the data reduction software GLITTER (van Achtenberg et al., 2001). Further data reduction including evaluation of the need of a common lead correction and error propagation was performed using in house excel spreadsheets. An age related common lead correction is needed when an analysis shows baseline-subtracted common lead contents significantly above the detection limit (i.e., > 50 cps). During this study of monazite and xenotime, common lead correction has not been applied since <sup>204</sup>Pb counts were not distinct from background in any analyses. Errors are propagated by quadratic addition of within-run errors (2 standard errors), the reproducibility of the standard during the analytical session (2 standard deviations) and the overall error on the certification of the standard used for that session. Plotting of the U–Pb isotopic data and age calculations were performed using the Isoplot/Ex 4.15 program (Ludwig, 2012). All ages were calculated with 2σ errors and without decay constants errors. Data point error ellipses in the figures showing results of analyses are at the 2σ level. Concentrations of U, Th and Pb

(total) in the unknowns were calculated from average blank subtracted mean count rates for each element measured on the standard used for that session. Grain to grain concentration variations in the standards limit the quality of these concentration data to  $\pm 20\%$ .

Multi-collector ICPMS analyses of zircon were performed according to Huhma et al. (2012) and calculations were made using software developed by T. Andersen (University of Oslo). All analyses of Pb isotopes in galena by the multi-collector ICPMS were made using laser

rasters with a stage stepping speed of 1  $\mu\text{m}/\text{second}$ . Ablation conditions were: 5  $\mu\text{m}$  beam diameter; 5 Hz pulse frequency; 1.4  $\text{J}/\text{cm}^2$  beam energy density. The MC-ICP-MS is equipped with 9 Faraday detectors and amplifiers with  $10^{11} \Omega$  resistors. Baseline and ablation data were measured on peaks ( $^{208}\text{Pb}$ ,  $^{207}\text{Pb}$ ,  $^{206}\text{Pb}$ ,  $^{204}\text{Pb}$ ,  $^{205}\text{Tl}$ ,  $^{203}\text{Tl}$ ) and collected in static mode. The raw data were filtered at 2 s and corrected for mass discrimination using an exponential law. The mass discrimination factor for Pb was determined using a  $\sim 20$  ppb Tl solution nebulized at



(caption on next page)

**Fig. 3.** Photographs and photomicrographs of polished slabs and sections of different types of veins and mineral assemblages in the Iso-Kuotko deposit. A – Type 1 arsenopyrite-pyrite-bearing quartz-carbonate-albite vein (polished slab). B – Type 2 quartz vein (polished thin section, transmitted light, crossed polars). C – fragments of Type 2 vein in Type 3 breccia vein with pyrrhotite matrix (polished slab). D – matrix-supported Type 3 breccia-vein with pyrrhotite matrix and round-resorbed quartz fragments (polished slab). E – close-up of the groundmass of a mafic volcanic rock sample with chlorite-carbonate alteration (transmitted light, polarizing microscope). Note the distribution of rutile needles according to crenulation. F – chlorite-carbonate alteration of the groundmass of a mafic volcanic rocks sample. Note the corroded-resorbed character of prophyroblastic carbonate grains (polarizing microscope, transmitted light, crossed polars) and foliation-parallel distribution of rutile crystals. G – intense chlorite-carbonate alteration along a Type 1 vein (polished thin section, transmitted light). H – strongly fractured arsenopyrite surrounded by massive pyrite in a Type 1 vein (polished thin section, reflected light). I – fractured arsenopyrite with native gold bearing pyrrhotite-chalcopyrite-native bismuth Type 3 breccia-vein mineral assemblage in fractures. Note partial replacement of arsenopyrite by other ore minerals (polished thin section, reflected light). J – partial replacement of arsenopyrite by pyrrhotite in a Type 1 vein. Note the native bismuth bearing vein in arsenopyrite and termination of this vein at the pyrrhotite field grown on the resorbed surface of arsenopyrite (polished thin section, reflected light). K – remnants of Fe-Mg-rich carbonate in a Type 2 quartz vein (polished thin section, crossed polars). L – netty-texture pyrrhotite partially replacing euhedral quartz along the boundaries of crystals in a re-opened Type 2 vein. Note disintegration and partial resorption of quartz (polished thin sections, plan-polarized transmitted light). M – native gold inclusions in a pyrrhotite-chalcopyrite assemblage of a Type 3 vein (polished thin section, reflected light). N – late carbonate (Cb2) replaces Fe-Mg-rich carbonate (Cb1) in a Type 1 vein (polished thin section, plan-polarized transmitted light). O – partial replacement of pyrrhotite by chalcopyrite, native bismuth and galena in a Type 3 vein (polished thin section, reflected light). Abbreviations for mineral names: Cb – carbonate, Qz – quartz, Chl – chlorite, Py – pyrite, Apy – arsenopyrite, Cpy – chalcopyrite, Po – pyrrhotite, Nat.Bi – native bismuth; Nat.Au – native gold, Gn – galena.

the same time as the sample, using a desolvating nebulizer. A single Pb-Pb measurement included 1 min baseline measurement (measure zero) prior to a batch of ratio measurements, each of the latter consisting of data acquisition for 45 s with laser on. Breaks in an analytical session, or refilling the Tl solution necessitated a new zero measure. Plotting of the Pb-Pb isotopic data was performed using the Isoplot/Ex 4.15 program (Ludwig, 2012). Model ages, as well as  $\mu$  and  $\kappa$  values were iterated with  $2\sigma$  errors and without decay constants errors using in house Excel worksheets. Since the time calculation is an implicit function, the distribution of the solution is obtained by a Monte-Carlo simulation.

For Re-Os dating, powdered mineral separates were obtained by drilling euhedral arsenopyrite crystals identified in polished slabs from drill cores. The separates were acquired using a small hand-held drill and working under a binocular microscope. Other powdered mineral separates were obtained by grinding hand-picked arsenopyrite grains from crushed ore samples. Weighed powder was combined with an isotopically distinct  $^{185}\text{Re}$ - $^{188}\text{Os}$ - $^{190}\text{Os}$  “double spike” and inverse *aqua regia* in a borosilicate ampoule (Carius tube), sealed and heated at 250 °C for 12 h. Oxidation of arsenopyrite and its equilibration with spike rhenium and osmium ensures accurate concentration data independent of analytical yield. Osmium is separated from the solution by solvent extraction into chloroform followed by back-extraction into hydrobromic acid (HBr). Subsequent micro-distillation provides a high purity Os split. Rhenium is extracted from the remaining inverse *aqua regia* solution by anion exchange chromatography. Purified Re and Os are loaded on outgassed Pt filaments for mass spectrometry. Isotopic ratios of Re and Os are measured on a Triton thermal ionization mass spectrometer (TIMS) at the AIRIE Program, Colorado State University. Barium activators enhance ion yield resulting in Re intensities that can be measured by Faraday cup, whereas Os intensities may be measured either by peak-hopping (secondary electron multiplier) or simultaneous Faraday cup collection, depending on signal strength. Both Re and Os are analysed as oxides with ratios corrected for oxygen isotopic systematics. The isotope dilution equation utilizing sample weight, spike weight, measured ratios, background “blank” information, and spike calibration data provides rhenium and osmium concentrations and isotopic ratios. Errors for each variable are fully propagated. Re and Os blanks are in the low picogram to femtogram range, with less than 1% contribution ( $\text{Re} = 1.04 \pm 0.08 \text{ pg}$ ,  $\text{Os} = 0.338 \pm 0.010 \text{ pg}$  with  $^{187}\text{Os}/^{188}\text{Os} = 0.275 \pm 0.011$ ).

## 4. Results

### 4.1. Alteration of host rocks, types of ore veins and geochemistry of ore

The orebodies in the Iso-Kuotko deposit consist of networks of plustage veins and breccias hosted by tholeiitic basalt lavas and tuffs, as well as felsic porphyry dikes metamorphosed in low greenschist

facies (Figs. 2 and 3A-D). The host rocks are characterised by chlorite-, carbonate-, Ti-oxide/silicate and sericite-dominated metamorphic recrystallization and vein-related alteration. In the massive, fine grained, originally aphanitic basalt, the groundmass is partially recrystallized to chlorite with occasional occurrences of subhedral-rhombohedral carbonate porphyroblasts which are arranged into foliation-parallel seams. Locally, abundant elongate ilmenite and titanite grains are also parallel with the crenulated foliation (Fig. 3 E and F). The groundmass also contains weakly disseminated pyrite and pyrrhotite pseudomorphs after euhedral pyrite. In the amygdular variety of basalt, the up to 4 mm amygdules are mostly filled by pyrrhotite, chalcopyrite and chlorite. In the mafic tuff, the mineralogy of metamorphic recrystallization varies according to the original heterogeneity in composition of the rock. There are mafic layers with chlorite rich groundmass hosting variable amounts of disseminated carbonate porphyroblasts and Ti-oxide minerals, whereas patchy to almost massive sericite predominates in layers with a more felsic original composition. Weakly disseminated pyrrhotite pseudomorphs after euhedral pyrite and chalcopyrite are also present in this rock. In the porphyritic felsic rock, plagioclase phenocrysts are variably replaced by sericite and carbonate minerals. Carbonate porphyroblasts are also present in the fine-grained quartz-feldspar-chlorite groundmass. The euhedral-subhedral carbonate rhombohedrons have corroded outlines where patches and masses of sericite replace the groundmass.

Hydrothermal veins and breccia bodies with gold mineralization occur in all rock types (Fig. 2). Carbonate and quartz are the predominant gangue minerals in veins and breccias; the abundance and compositions of ore mineral assemblages are highly variable. The mafic host rocks usually show a few centimeter wide very intense carbonate-chlorite alteration along the early veins (see below and Fig. 3G). Intense sericitisation is also present in the alteration selvages of quartz-dominated veins in felsic rocks. As the drill cores are not oriented, the true orientation of the sampled veins and breccias cannot be determined. However, temporal relationships between the different types of veins, breccias and deformation features in host rocks could be evaluated by petrography.

The veins and breccia bodies cut across the crenulated foliation of the host rocks suggesting that their formation post-dated the regional D1-D2 ductile deformation stages. According to mineralogy, texture and cross cutting relationships, three types of veins were distinguished:

Type 1, early quartz-carbonate-albite veins with arsenopyrite and pyrite (Fig. 3A). The apparent width of these veins in the drillcores is highly variable from less than 1 cm to up to 50 cm. In the thicker veins, arsenopyrite locally forms massive aggregates of up to 2 cm large, slightly resorbed and fractured, euhedral-subhedral grains. Fractures of arsenopyrite are filled up by the quartz-carbonate matrix of the veins. Euhedral pyrite is either disseminated in the vein filling carbonate and quartz (Fig. 3G) or attached to arsenopyrite in massive aggregates



(Fig. 3A and H), but it also occurs in the fractures of arsenopyrite. The vein filling carbonate has Mg- and Fe-rich compositions (dolomite-ferro-dolomite-ankerite). The subhedral-anhedral quartz grains show strong undulose extinction and development of subgrains along grain boundaries suggesting that deformation affected these veins. Albite is a subordinate constituent in these veins and forms aggregates of radially arranged or comb-textured small prisms (10–100 µm wide) on the vein walls. Carbonate-chlorite alteration selvages are common around Type 1 veins (Fig. 3G).

Type 2 veins with fine to coarse grained massive, locally comb textured and drusy infillings of quartz (Fig. 3B). The size of quartz crystals/grains is up to 1–2 cm and the apparent width of veins is variable from millimeter to centimetre range. In some of these quartz-dominated veins, the coarse quartz grains enclose resorbed fields of Fe-Mg-rich carbonate, pyrite and arsenopyrite which are the remnants the Type 1 veins (Fig. 3K); this texture suggest that some of Type 2 veins were formed by re-activation of Type 1 veins. The felsic host rocks show up to 1 cm-wide sericite rich alteration along these quartz-dominated veins and sericite flakes and seams of sericite also occur within the veins and quartz grains. As in Type 1 veins, quartz show undulose extinction and mosaic-textured fine-grained masses of sub-grains occur between the coarse grained subhedral-anhedral crystals. Albite is a subordinate constituent in these veins and forms aggregates of radially arranged or comb-textured small prisms (10–100 µm wide) on the vein walls.

Type 3, breccia-veins with massive pyrrhotite matrix hosting fragments of Type 1 and Type 2 veins and rare fragments of wall rocks (Fig. 3C and D): the shape and size of fragments and their volume ratio to the matrix is highly variable and gradual development of the breccia from the earlier formed Type 1 and Type 2 veins can also be followed in several drill core intercepts. The incipient stage of breccia formation is characterised by replacement of sulphides along fractures and grain boundaries of quartz, carbonate and sulphide minerals (Fig. 3I). In the more developed breccias, the mineral grains or composite fragments have been dispersed, but their original positions and contacts are still recognisable (Fig. 3J and L). In the matrix supported, fully developed breccias, the mineral and vein fragments have resorbed-rounded shapes and their outlines no longer match each other (Fig. 3D). These textural features suggest that the preferred sites of brecciation were the previously formed veins and these late breccias predominantly formed by re-opening of earlier veins. The massive sulphide matrix of the breccia predominantly consists of pyrrhotite which also encloses some euhedral up to 2 cm large sparry calcite rhombohedrons. These calcite crystals encloses remnants of Fe-bearing dolomite from the early veins (Fig. 3N). Chalcopyrite, sphalerite and pentlandite are accessory minerals and are enclosed in pyrrhotite. In some pyrrhotite grains, the presence of native gold inclusions was also detected (Fig. 3M). Thin (0.1–5 mm) fractures cutting through pyrrhotite in the matrix and other minerals in the fragments are also preferred sites of native gold occurrences. Native gold is associated with native bismuth, bismuthinite, galena and calcite in these fractures (Fig. 3I and O). Native bismuth-bismuthinite-galena patches also replace pyrrhotite in the matrix and pyrite and arsenopyrite in the fragments, as well as fills up thin (< 1mm), short fractures penetrating the wallrock along veins and intercrystalline spaces of early veins in the marginal zones of breccias. However, these fracture fillings are partly synchronous with the formation of breccias because some of them terminate along the mineral fragment/pyrrhotite matrix boundaries (Fig. 3J), whereas others cut through pyrrhotite (Fig. 3O) and calcite grains in the matrix. Ore minerals predominate in these fractures where they cut other, sulphide minerals (e.g., arsenopyrite in Type 1 veins; Fig. 3I), whereas calcite is the dominant vein fill at other places. Specific hydrothermal alteration cannot be connected to Type 3 veins. As they represent re-activated and brecciated earlier veins, the carbonate-chlorite-sericite alteration around them was probably formed during the earlier veining events.

According to the observed cross-cutting relationships and textures of mineral parageneses, the relative timing of deposition of minerals

and major stages of gold deposition can be determined (Fig. 4). Observations support formation of gold mineralization in two major stages. Type 1 arsenopyrite bearing veins with refractory gold represent the first stage. Type 1 veins were re-activated and locally brecciated, and their minerals were fractured and partially replaced by the minerals of Type 2 and Type 3 veins. Type 2 veins are barren and they are also partially replaced-brecciated-cemented by the minerals of Type 3 veins carrying free gold.

The most important feature of the multi-stage mineralization in the Iso Kuotko deposit is the association of visible gold with the late stage brittle fracturing and brecciation. In agreement with the petrographic observations, the correlation of gold and bismuth concentrations in the drill cores (Fig. 2) confirms that the major stage of gold deposition can be connected to the late Bi-mineral bearing veins. A well-defined correlation between concentrations of gold and arsenic does not exist: both high and low arsenic concentrations occur in high Au-grade zones. The local association of high gold and arsenic grades can be attributed to the partly refractory nature of gold mineralization (e.g. gold is concentrated in the crystal structure of the early arsenopyrite and pyrite; Härkönen et al., 2000) and partly to the local presence of late fractures with native gold in Type 1 veins.

#### 4.2. Morphology, texture, composition and U-Pb age data for hydrothermal monazite

Monazite was found with varying grain size depending on mode of occurrence (Fig. 5A; Fig. 6A). In the strongly altered mafic volcanic rock, only small, usually less than 50 µm in length, inclusion rich, anhedral-subhedral hydrothermal monazite grains were detected (sample #1316960 and #1316965; Fig. 2). We attempted U-Pb age dating on the small inclusion-free areas of this type of monazite by decreasing the diameter of the laser beam to 10 µm. Smaller laser spot-sizes (5–10 µm) provide better spatial resolution for analysing single, isotopically homogenous domains and limits contact with inclusion/fractures (Paquette and Tiepolo, 2007), but this analytical setup resulted in very low  $^{207}\text{Pb}$  count rates (< 1300 cps) and large, up to 3% relative errors on the  $^{207}\text{Pb}/^{206}\text{Pb}$  ratios. This reflects low signal/background ratio and the hydrothermal origin of monazite grains, which are comparatively deficient in both U (< c. 0.2 wt%) and Th (< c. 1 wt%) relative to igneous or high grade metamorphic monazite (Schandl and Gorton, 2004; Zhu and O'Nions, 1999). Consequently, the data from monazites from the altered rocks are too imprecise to make any conclusions and are not discussed further in this study.

Monazite also occurs in the Type 1 veins as up to 2 mm large, strongly fractured-altered euhedral crystals (Fig. 5A). In the cores of this type of monazites (sample 22051503F), the irregular-patchy distribution of brighter and darker fields on FE-SEM images indicate heterogeneous chemical composition. These cores are also rich in inclusions of pyrite, carbonate, albite, and occasionally, also contain xenotime and thorite inclusions, and show porosity and fracturing (Figs. 5B and 6B-C). On the other hand, monazite also occurs as inclusion in pyrite, confirming that the growth of monazite cores was synchronous with the formation of the early, Type 1 veins. The rims of monazite exhibit oscillatory chemical zoning and the porosity and inclusion density is minimal; localised minor alteration, which resulted in the change of composition of monazite and disturbance of oscillatory zoning is seen along fractures only (e.g. the lower right area in the large monazite crystal shown on Fig. 6B).

The variations in chemical compositions along profiles across dark and bright areas and growth zones in the core and rim of a large monazite grain (Fig. 6B) in sample 22051503F are shown on Fig. 7. Data are listed in Electronic Material Table 1. There are no significant differences in terms of  $\text{Ce}_2\text{O}_3$ ,  $\text{P}_2\text{O}_5$ ,  $\text{SiO}_2$ ,  $\text{Y}_2\text{O}_3$ ,  $\text{FeO}$ ,  $\text{CaO}$ ,  $\text{F}$  and  $\text{Cl}$  concentrations between the core and rim. Fluorine has much higher concentrations (0.54–1.29 wt%) both in core and rim compared to chlorine (0.03–0.05 wt%). As typical for monazite, the light REEs

		Stage I gold REFRACTORY GOLD		Stage II gold FREE GOLD
		Type 1 veins	Type 2 veins	Type 3 veins
Ore minerals	Mineral			
	Arsenopyrite	██████████		
	Pyrite		██████████	
	Pyrrhotite			██████████
	Chalcopyrite			██████████
	Galena			██████████
	Native bismuth			██████████
	Bismuthinite			██████████
	Native gold			██████████
	Maldonite			██████████
Gangue and alteration minerals	Quartz	██████████	██████████	
	Carbonate	██████████		██████████
	Albite	██████████	██████████	
	Chlorite	██████████		
	Sericite	██████████	██████████	
	Rutile	██████████		
Accessory phosphate minerals	Monazite	██████████		
	Xenotime	██████████	██████████	██████████

Fig. 4. Mineral paragenesis in veins and altered host rocks.

(Ce<sub>2</sub>O<sub>3</sub>, La<sub>2</sub>O<sub>3</sub>, Pr<sub>2</sub>O<sub>3</sub>, Nd<sub>2</sub>O<sub>3</sub>, Sm<sub>2</sub>O<sub>3</sub> and Gd<sub>2</sub>O<sub>3</sub>) have higher concentrations in comparison to the heavy REEs (Tb<sub>2</sub>O<sub>3</sub>, Dy<sub>2</sub>O<sub>3</sub>, Ho<sub>2</sub>O<sub>3</sub>, Er<sub>2</sub>O<sub>3</sub>, Yb<sub>2</sub>O<sub>3</sub>, Lu<sub>2</sub>O<sub>3</sub>), and concentrations for most of the heavy REEs are below the detection limits of the microprobe. Except for Ce<sub>2</sub>O<sub>3</sub>, concentrations of the light REEs show significant differences in the core

and rim of the crystal. The concentrations of La<sub>2</sub>O<sub>3</sub> in the core are between 18.3 and 18.6 wt%, whereas the rim has lower values, from 15.7 to 16.8 wt%. Nd<sub>2</sub>O<sub>3</sub> and Gd<sub>2</sub>O<sub>3</sub> show higher concentrations in the rim (10.1–11.3 wt% and 0.54–0.92 wt%, respectively) than in the core of the crystal (9.12–9.60 wt% and 0.45–0.58 wt%, respectively) and

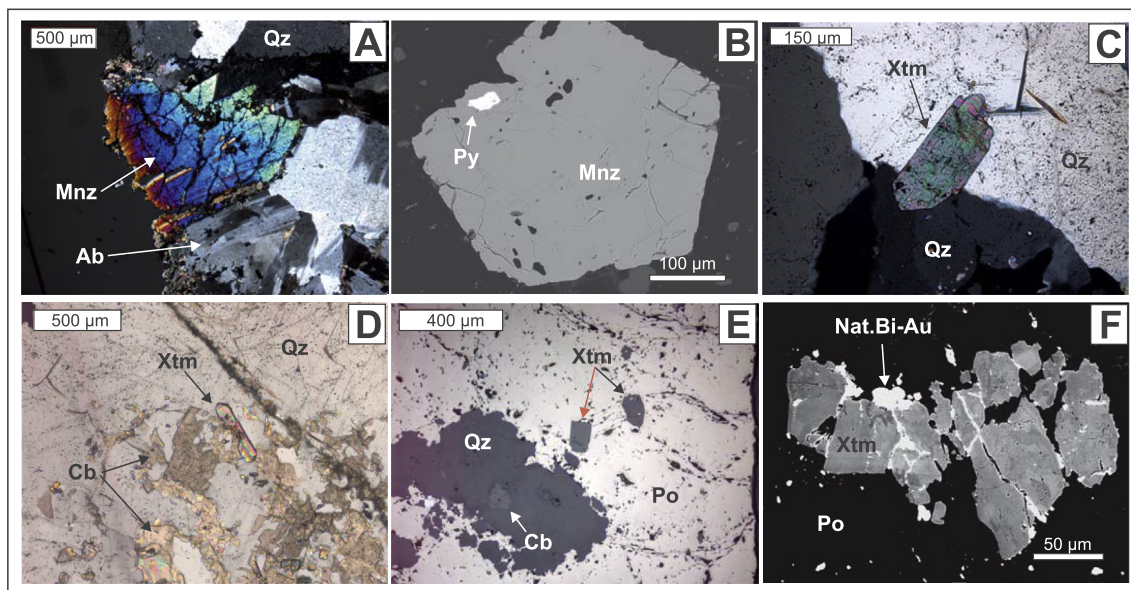
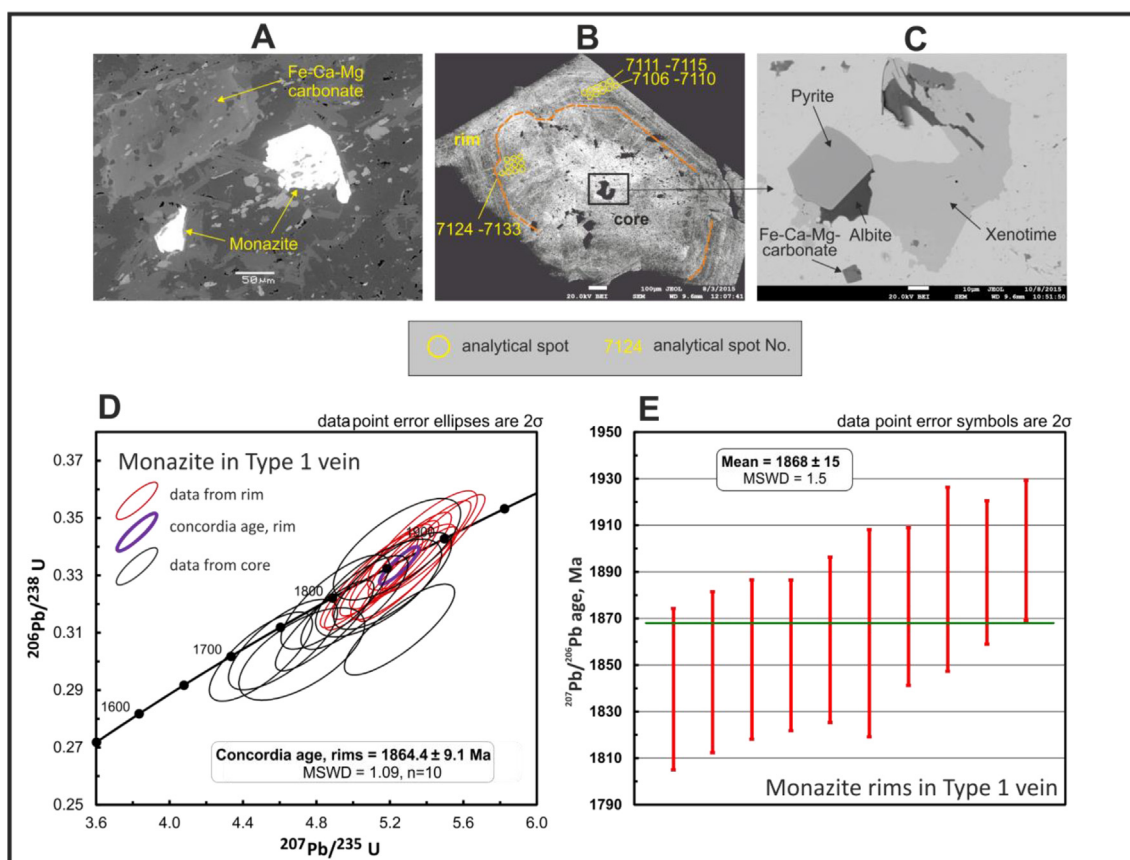
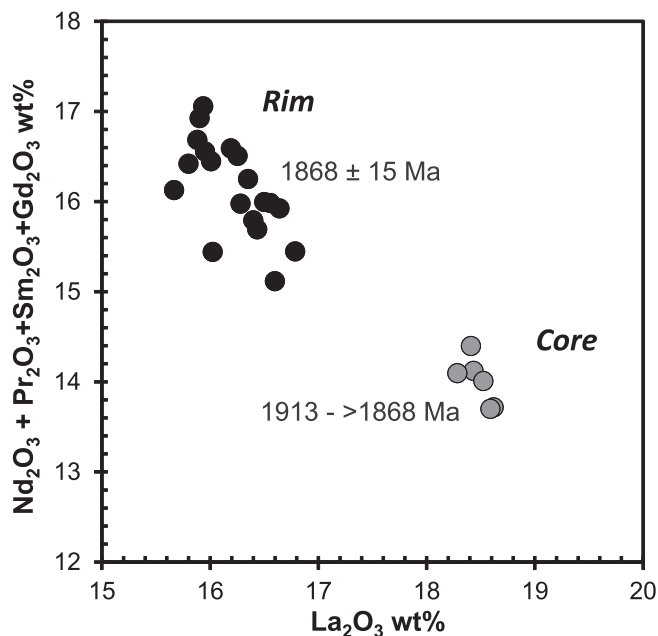


Fig. 5. Textural settings and types of hydrothermal monazite and xenotime in the veins. A – fractured-altered monazite in a Type 1 vein (transmitted light, crossed polars). B – pyrite inclusion in monazite from a Type 1 vein (SEM backscattered electron (BSE) image). C – Type A xenotime along grain boundaries of quartz in a Type 2 vein (transmitted light, crossed polars). D – Type A euhedral xenotime attached to relict Fe-Mg-rich carbonate from a Type 2 vein (transmitted light, crossed polars). The SEM-BSE image of this grain with a relict core is shown on the Fig. 8C. E – Type C euhedral-subhedral xenotime crystals enclosed by pyrrhotite in a Type 3 vein (reflected light). SEM-BSE image of this grain is shown on Fig. 9A. F – Type B fractured xenotime in pyrrhotite from a Type 3 vein (SEM-BSE image). Note the heterogeneous-patchy composition of xenotime. Fractures in xenotime are filled in by the native bismuth-natural gold bearing mineral assemblages. Abbreviations for mineral names: Cb – carbonate, Qz – quartz, Ab – albite, Py – pyrite, Po – pyrrhotite, Nat.Bi – native bismuth; Nat.Au – native gold, Mnz – monazite, Xtm – xenotime.



**Fig. 6.** Texture of monazite (FE-SEM-BSE images) and results of U-Pb dating. A – inclusion-rich monazite in the altered mafic volcanic rock. This kind of monazite is not useful for U-Pb dating (see text for explanation). B – large monazite grain in a Type 1 vein from the sample #22150503F. Note the heterogeneous-patchy composition and inclusion-rich nature of the core and the oscillatory growth zoning in the rim. C – close-up of inclusions in the core of the monazite crystal shown in Fig. 6B. D – U-Pb concordia diagram for the monazite shown on the Fig. 6B. E – individual  $^{207}\text{Pb}/^{206}\text{Pb}$  concordant data used in calculation of weighted mean age.



**Fig. 7.** Light REE (except for  $\text{Ce}_2\text{O}_3$ ) concentrations in the core and rim of monazite shown on the Fig. 6 B. Data are listed in Electronic Material Table 3.

this relationship also exists for the concentrations of the other light REEs, thus there is a significant difference between the total analysed light REE contents in the rim and core (Fig. 7). The concentrations of U

and Pb are below detection limits of microprobe.  $\text{ThO}_2$  shows a wider range of variation from 0.20 to 1.30 wt% in the oscillatory growth zones of the rim than in the irregularly heterogeneous core where the  $\text{ThO}_2$  concentrations are between 0.20 and 0.56 wt% (Electronic Material Table 1). The generally low  $\text{ThO}_2$  concentrations are typical for monazite of hydrothermal origin (Schandl and Gorton, 2004).

The results of U-Pb age dating of monazite are listed in Electronic Material Table 2 and shown on Fig. 6D and E. From the heterogeneous core, most of the results are either scattered or discordant, giving unreliable age data with large errors and hence we do not consider these data for further evaluation. However, all analytical spots from the oscillatory zoned rim provided concordant (e.g. the calculated concordance % values are between 95 and 105) and consistent data. The concordia age for these spots is  $1864.4 \pm 9.1$  Ma (MSWD = 1.09; Fig. 6) and the weighted mean  $^{207}\text{Pb}/^{206}\text{Pb}$  age is  $1868 \pm 15$  Ma (MSWD = 1.5).

#### 4.3. Morphology, texture, composition and U-Pb age data for hydrothermal xenotime

Xenotime of sufficient size (e.g.  $> 50 \mu\text{m}$ ) for U-Pb age dating by the applied LA-ICPMS method was found in Type 2 and Type 3 veins (Fig. 4). This accessory phosphate mineral occurs in four morphological-textural varieties in these veins. Type A xenotime is hosted by quartz in Type 2 veins (samples #1316958, #1316967, #1316968, #1316969, Figs. 2 and 5C-D). It is characterised by subhedral-euhedral outlines and distinctive core-rim internal texture (Fig. 8A-C). The cores of these crystals have subhedral to irregular shapes and irregular-patchy distribution of compositionally different dark and brighter areas

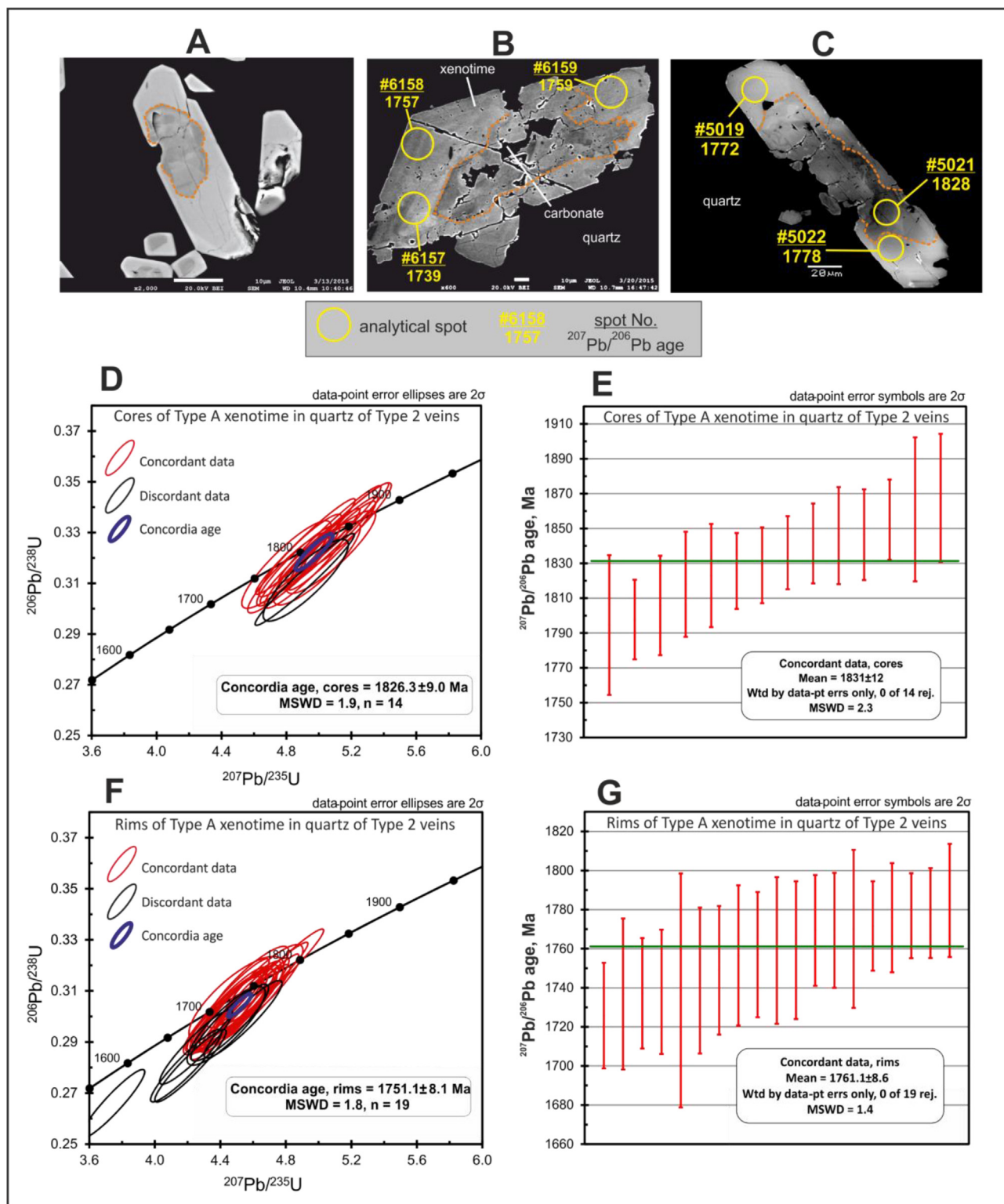


**Fig. 8.** Texture of quartz-hosted Type A xenotime in Type 2 veins (FE-SEM-BSE images) and results of U-Pb dating. A – xenotime with patchy-heterogeneous composition in the core and homogeneous composition in the rim. B – xenotime with inclusion-rich and heterogeneous core and inclusion-free rim with oscillatory growth zoning. C – xenotime with heterogeneous composition in the core and homogeneous rim. D – concordia diagram showing U-Pb data from core analyses. E – weighted mean of <sup>207</sup>Pb/<sup>206</sup>Pb ages based on concordant data in diagram to left. F – concordia diagram showing U-Pb data from rims. G – individual <sup>207</sup>Pb/<sup>206</sup>Pb concordant data used in calculation of weighted mean age.

in backscattered electron images. An abundance of carbonate inclusions and intense fracturing are also typical for these cores. The rims of these crystals are homogeneous or show faint oscillatory zoning. Type B xenotime grains are enclosed by pyrrhotite in Type 3 veins are

characterised by irregular-patchy compositional heterogeneity, resorbed-irregular outlines, intense fracturing, and occurrence of native bismuth in fractures (samples # 13169\_58 and 1316969; Figs. 5F and 9B-C). The rest of xenotime grains (Type C) in the pyrrhotite masses of

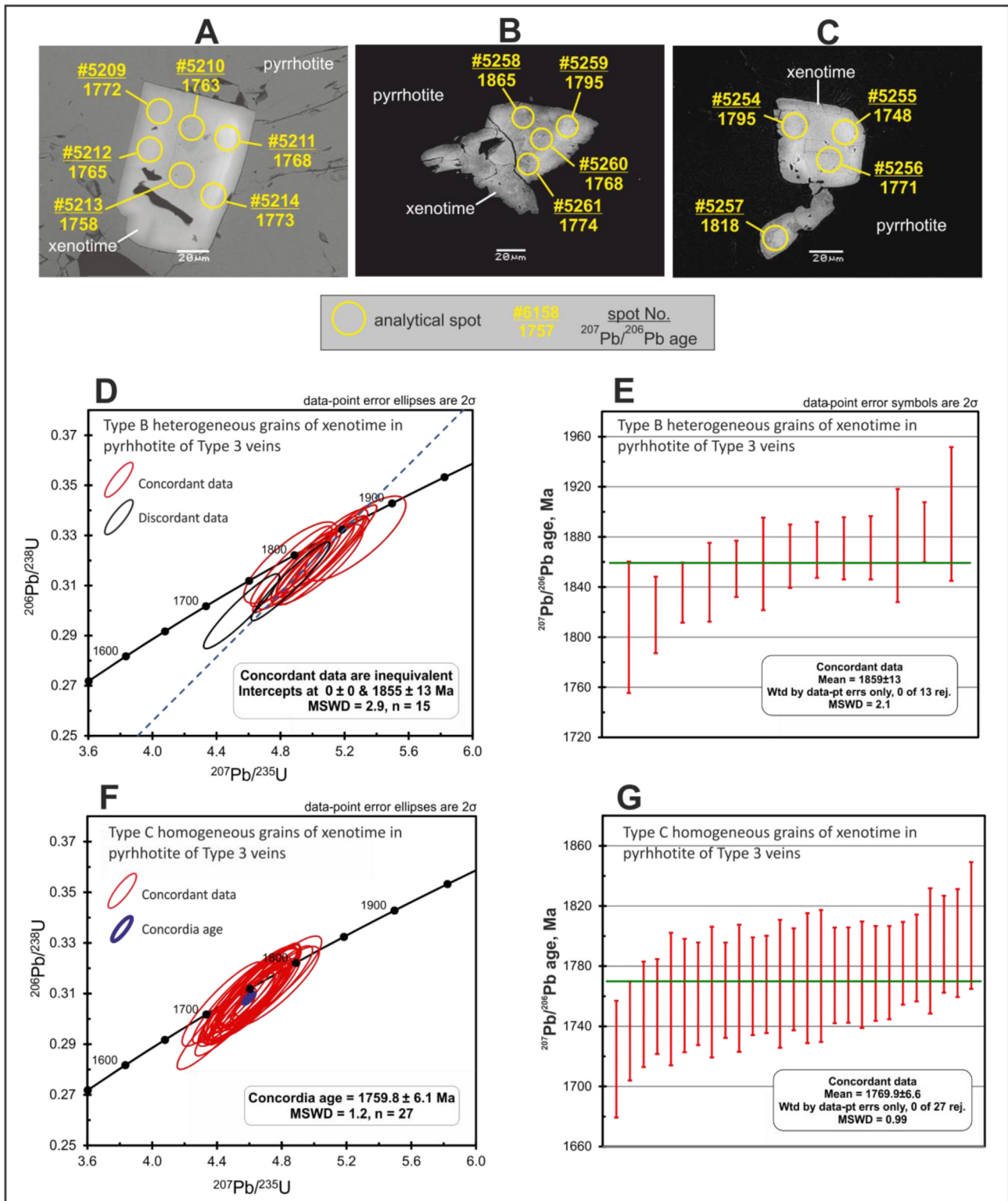


**Fig. 9.** Texture of pyrrhotite-hosted Type B and C xenotime in Type 3 veins (FE-SEM-BSE images) and results of U-Pb dating. A – euhedral Type C xenotime with largely homogeneous composition (faint oscillatory growth zoning). B – subhedral, resorbed Type B xenotime with patchy-heterogeneous composition. C – slightly resorbed euhedral Type C xenotime grain with homogeneous composition (faint oscillatory zoning) and a subhedral-resorbed Type B xenotime with patchy-heterogeneous composition (lower part of the picture). D – concordia diagram showing U-Pb data for Type B heterogeneous grains. E – weighted mean error for  $^{207}\text{Pb}/^{206}\text{Pb}$  ages based on concordant data to left. F – concordia diagram showing U-Pb data for Type C homogeneous grains and grains with faint oscillatory growth zoning. G – individual  $^{207}\text{Pb}/^{206}\text{Pb}$  concordant data used in calculation of weighted mean age.

Type 3 veins is euhedral to angular-fragmented. This type of xenotime is homogeneous or show faint oscillatory zoning according to observations by SEM (Figs. 5E and 9A). Type D xenotime inclusions in the

sparry carbonate of Type 3 veins (samples #1316958 and #1316959; Fig. 2) are euhedral-fragmented with well-developed oscillatory growth zoning (Fig. 10A–C).

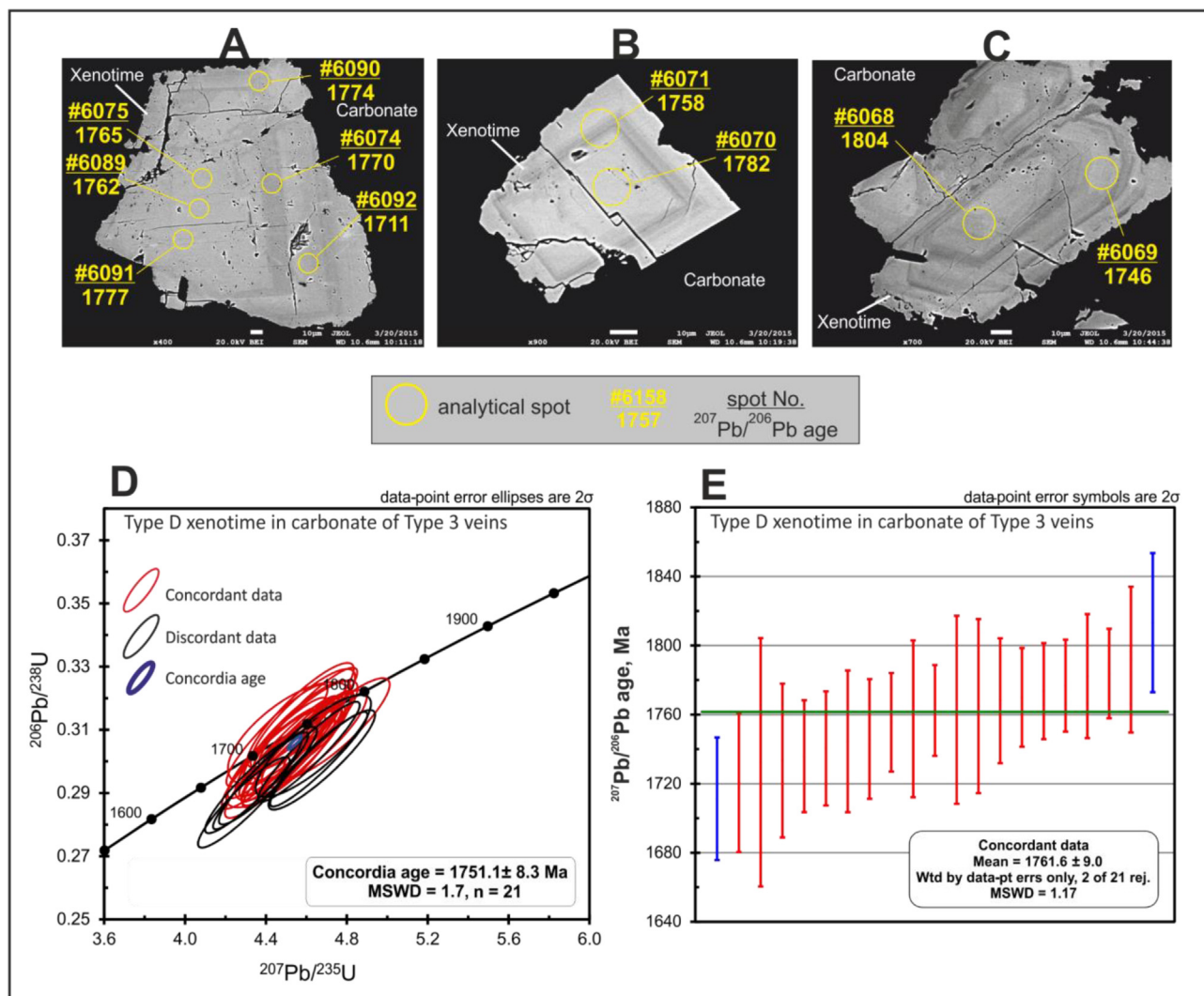


**Fig. 10.** Texture of the carbonate-hosted Type D xenotime in Type 3 veins (FE-SEM-BSE images) and results of U-Pb dating. A-C euhedral to subhedral Type D xenotime grains with oscillatory growth zoning. D – concordia diagram showing U-Pb data for Type D xenotime grains. E – individual  $^{207}\text{Pb}/^{206}\text{Pb}$  concordant data used in calculation of weighted mean age. Data marked by blue error bars are rejected in calculation of weighted mean age. (For interpretation of the references to colour in this figure legend, the reader is referred to the web version of this article.)

Chemical compositions of xenotime grains in Type 2 and Type 3 veins are listed in the [Electronic Material Table 3](#) according to their host minerals and zoning. Lower than the expected totals of 94.5–97.3 wt% may result from the presence of water, crystalline nano-pores or, less likely, elements not included in the analytical procedure, such as europium and hexavalent uranium (Förster, 2006; Seydoux-Guillaume et al., 2012). Xenotime grains have typical  $\text{Y}_2\text{O}_3$ ,  $\text{P}_2\text{O}_5$  and  $\text{EREE}_2\text{O}_3$  (wt %) ranges of 37.5–42.4, 32.7–33.8 and 60.6–63.1, respectively. Other than  $\text{Y}_2\text{O}_3$ ,  $\text{EREE}_2\text{O}_3$  values are dominated by  $\text{Gd}_2\text{O}_3$  (average 6.66 wt %),  $\text{Dy}_2\text{O}_3$  (average 7.01 wt %) and  $\text{Er}_2\text{O}_3$  (av. 3.43 wt %). The low U and Th concentrations support a hydrothermal origin for xenotime (Kositcin et al., 2003; Zi et al., 2015). Xenotime of hydrothermal origin can also be distinguished from magmatic and detrital xenotime based on C1 chondrite normalised  $\text{Gd}_N$  and  $\text{Yb}_N$  concentrations (Kositcin et al., 2003; Rasmussen et al., 2011). Xenotime grains from the Iso-Kuotko deposit have  $\text{Gd}_N$  values larger than 200 000 and  $\text{Gd}_N/\text{Yb}_N$  values larger than 1, which are consistent with a hydrothermal origin (Fig. 11A). The compositions of some of the cores of Type A xenotime and some grains of Type B xenotime form a distinct population compared to the rest of cores and heterogeneous grains. The latter group have similar compositions to the rims of Type A xenotime and to the grains of Type D xenotime. Similar relationships can be seen on the

$\text{Y}_2\text{O}_3$  wt% vs.  $\text{Sm}_2\text{O}_3/\text{Yb}_2\text{O}_3$  wt% diagram (Fig. 11B).

U-Pb age dating of xenotime was performed according to different types of veins and the textural peculiarities of xenotime. Except for two spots, all analysed areas in the cores of quartz-hosted xenotime in Type 2 veins provided concordant data (Electronic Material Table 4). The calculated concordia age for these xenotime cores is  $1826.3 \pm 9.0$  Ma (MSWD = 1.9; Fig. 8D) and the weighted mean  $^{207}\text{Pb}/^{206}\text{Pb}$  age is  $1831 \pm 12$  Ma (MSWD = 2.3; Fig. 8E). About 70% of analyses in the rims of quartz-hosted Type A xenotime provided concordant data (Electronic Material Table 4). The concordia age is  $1751.1 \pm 8.1$  Ma (MSWD = 1.9; Fig. 8F). The weighted  $^{207}\text{Pb}/^{206}\text{Pb}$  age is  $1761.1 \pm 8.4$  (MSWD = 1.4; Fig. 8G).

Some analytical spots in the heterogeneous-resorbed grains of Type B xenotime inclusions in pyrrhotite of Type 3 veins also provided concordant U-Pb data (Electronic Material Table 5; Fig. 9D). However, these data are internally not consistent. Therefore calculation of a concordia age was not possible. By setting the lower concordia intercept to  $0 \pm 0$  Ma, Mode I regression (Ludwig, 2012) using all analytical data provided  $1855 \pm 13$  Ma (MSWD = 2.9) upper intercept age. The weighted  $^{207}\text{Pb}/^{206}\text{Pb}$  age for the concordant data is  $1859 \pm 13$  Ma (MSWD = 2.1; Fig. 9E). All U-Pb data obtained from the homogeneous Type C xenotime inclusions in pyrrhotite are concordant (Electronic

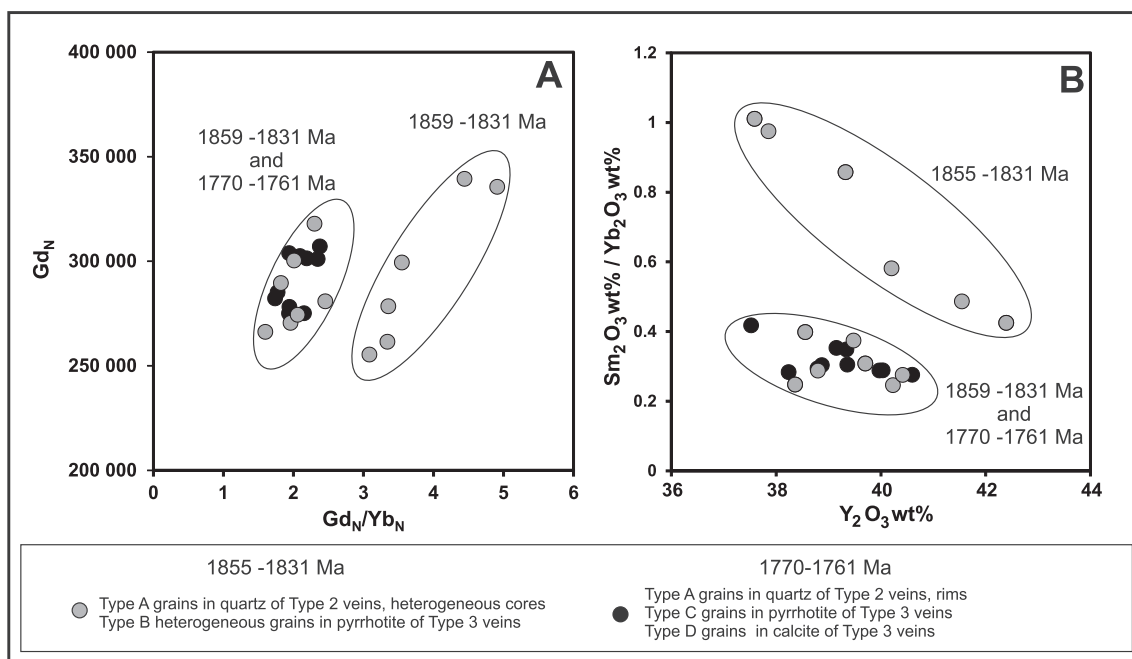


**Fig. 11.** Gd-Yb-Sm compositions of types of xenotime from Type 2 and Type 3 veins. Data in [Electronic Material Table 4](#). A – chondrite-normalized gadolinium versus chondrite-normalized gadolinium/ytterbium ratio plot. B – samarium-oxide/ytterbium oxide ratio versus yttrium-oxide plot.

[Material Table 5](#)). The concordia age for these grains is  $1759.8 \pm 6.1$  Ma (MSWD = 1.2; [Fig. 9F](#)) and the weighted mean  $^{207}\text{Pb}/^{206}\text{Pb}$  age is  $1769.9 \pm 6.6$  (MSWD = 0.99; [Fig. 9G](#)).

Most Type D xenotime crystals with oscillatory growth zoning from the sparry carbonate infill of Type 3 veins also provided concordant U-Pb data ([Electronic Material Table 6](#)). The concordia age is  $1751.1 \pm 8.3$  Ma (MSWD = 1.7; [Fig. 10D](#)), whereas the weighted mean  $^{207}\text{Pb}/^{206}\text{Pb}$  age is  $1761.6 \pm 9.0$  Ma (MSWD = 1.17; [Fig. 10E](#)).

#### 4.4. U-Pb geochronology of rock forming zircon separates from felsic porphyry dikes

Previous studies by [Mänttari \(1998\)](#) determined an imprecise  $1915 \pm 55$  Ma (MSWD = 160; sample A1262) U-Pb age on a zircon separate from a mineralized felsic porphyry dike in the Kati ore body by using the TIMS analytical technique. During our current studies, we used grains from the same zircon separate but performed spot analyses by LA-ICPMS. One zircon separate (A1669) from a mineralized felsic dike sample from the Suurikuusikko deposit was also included in the current studies in order to have a basis for comparison to data from the felsic dike from the Iso-Kuotko deposit and data obtained by [Rastas et al. \(2001\)](#) and [Ahtonen et al. \(2007\)](#) from the Ruoppapalo pluton ([Fig. 1A](#)).

In both samples, the 100–200  $\mu\text{m}$  large zircon crystals have euhedral-short prismatic appearance with approx. 1:1 to 3:1 aspect ratio. SEM back-scattered images show a clear core-rim zoning with large homogeneous bright cores and heterogeneous-porous, c. 10  $\mu\text{m}$  thin darker rims ([Fig. 12A-C](#) and [F](#)). Occasional heterogeneities in the cores occur as similarly dark-coloured patches along fractures ([Fig. 12C](#)), suggesting localised post-crystallization alteration, possibly by the hydrothermal processes leading to the alteration of the host rock and formation of the veins and breccias. The formation of the heterogeneous rims on the homogeneous cores can also be connected to the hydrothermal processes. However, the thin rims did not offer enough large areas to check their U-Pb ages by the analytical tools available for the purpose of this study. The U-Pb age data from the fracture-free homogeneous areas in zircon crystals are tabulated on the [Electronic Material Table 7](#) and shown on [Fig. 12D-E](#) and [G-H](#).

All analytical spots in zircons from the Iso-Kuotko deposit provided concordant and highly consistent data ([Fig. 12D](#)) and the calculated concordia age is  $1912.9 \pm 3.6$  Ma (MSWD = 4.8). The weighted mean average of  $^{207}\text{Pb}/^{206}\text{Pb}$  age is  $1913.5 \pm 3.5$  Ma (MSWD = 0.80; [Fig. 12E](#)). This result is more precise in comparison to the previously determined  $1915 \pm 55$  Ma (MSWD = 160) U-Pb age for this sample ([Mänttari, 1998](#)), because the applied analytical technique allowed exclusion of rims and heterogeneous areas of the zircon crystals.

In the zircon grains from the Suurikuusikko deposit, data are also concordant but highly scattered into several populations ([Fig. 12G](#)). 16 analyses by LA-MCICPMS give a range of ages from 1.9 to 2.8 Ga. The six youngest consistent data give a concordia age of  $1917 \pm 4$  Ma (mean  $^{207}\text{Pb}/^{206}\text{Pb}$  age is  $1916.3 \pm 6.6$  Ma, MSWD = 2.3; [Fig. 12H](#)) which is likely the maximum magmatic age of the dyke. The other grains are most probably inherited from the Archaean and Paleoproterozoic basement rocks, as their ages between 2.5 and 2.8 Ga are older than the mafic metavolcanic rocks of the Kittilä Group that is cut by the felsic dike.

#### 4.5. Pb isotopes in galena

Galena is useful for Pb-isotope studies because it preserves the lead isotopic ratios from the time of crystallization; e.g. the present-day lead isotope ratios measured in this mineral depend on the sources of metals and the age of crystallization only. This unique ability is related to the crystal structure of galena, which has such a very limited capacity to accommodate very small concentrations of uranium and thorium that the amounts of radiogenic lead produced by their radioactive decay essentially do not modify the initial “common” lead isotope ratios. Application of *in situ* LA MCICPMS eliminates the effect of potentially incomplete physical separation of galena from other sulphide minerals in aliquots used in bulk analytical methods ([Molnár et al., 2016](#)).

Galena is commonly associated with native gold, native bismuth and other minerals in the pyrrhotite-rich Type 3 veins at the Iso-Kuotko deposit ([Fig. 13A](#)). Pb-isotope ratios obtained from 31 galena grains from the ISO-12010 drillhole (samples from the 154.2 and 162.2 m depths; [Fig. 3](#)) show very little variation: the  $^{206}\text{Pb}/^{204}\text{Pb}$ ,  $^{207}\text{Pb}/^{204}\text{Pb}$  and  $^{208}\text{Pb}/^{204}\text{Pb}$  ratios are from 15.138 to 15.214, from 15.069 to

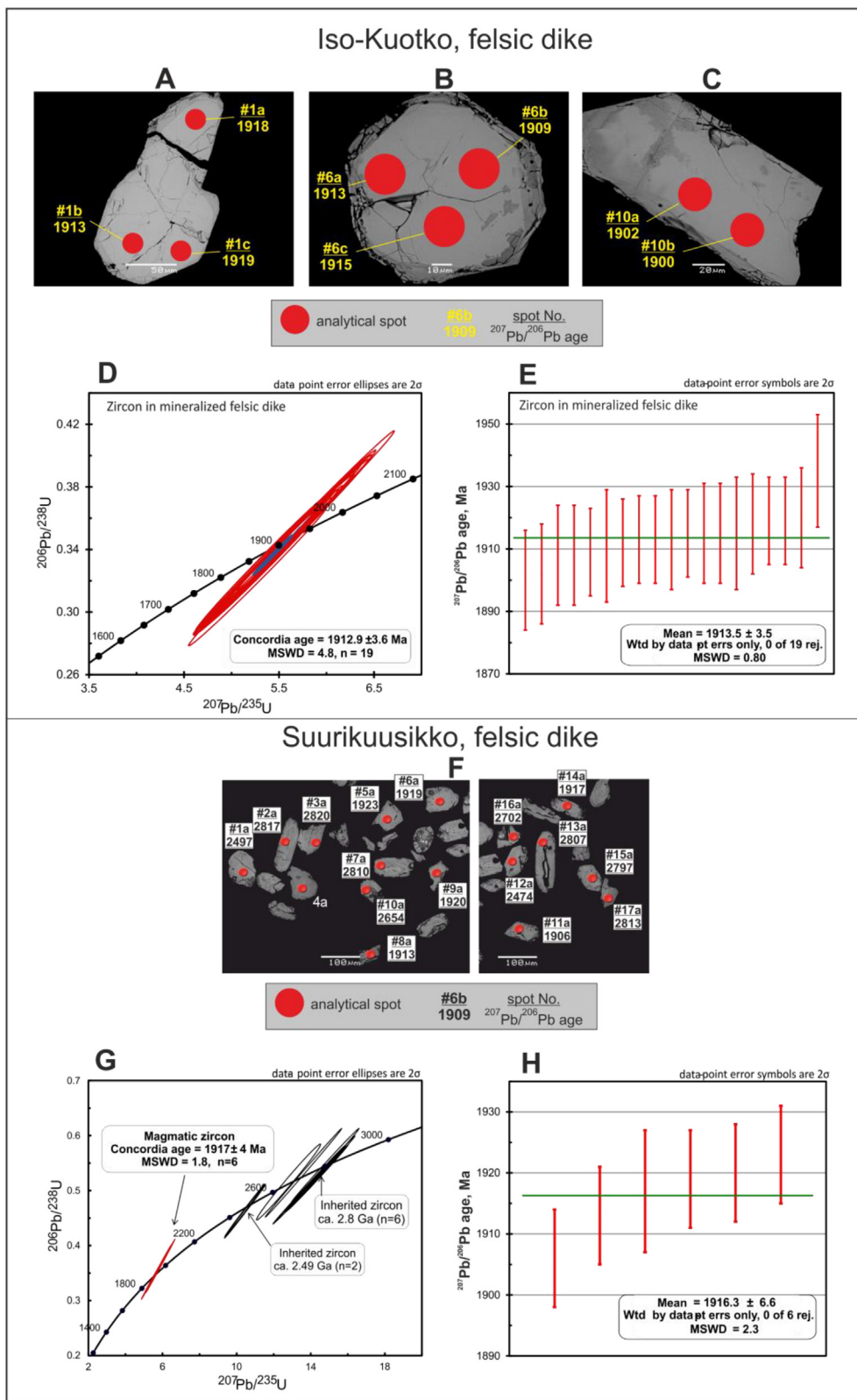


**Fig. 12.** Texture of zircons (FE-SEM-BSE images) and zircon U-Pb data from mineralized felsic dikes at the Iso-Kuotko (sample A1262; A-E) and Suurikuusikko (sample A1669; F-H) gold deposits. A-C euhedral to subhedral zircon grains with largely homogeneous cores and compositionally different thin rims, Iso-Kuotko. Heterogeneity in the cores occur along fractures. D – concordia diagram showing U-Pb data for heterogeneous grains, Iso Kuotko. E – individual  $^{207}\text{Pb}/^{206}\text{Pb}$  concordant data used in calculation of weighted mean age. (Iso Kuotko). F – zircon grains with compositional and core-rim zoning (Suurikuusikko); G – concordia diagram showing U-Pb data for heterogeneous grains, Suurikuusikko; H – individual  $^{207}\text{Pb}/^{206}\text{Pb}$  concordant data used in calculation of weighted mean age. (Suurikuusikko).

15.099, and from 34.759 to 34.852, respectively (Electronic Material Table 8). These compositions are slightly poorer in radiogenic lead compared to the results of previous TIMS analyses on two galena grains from the deposit by Mänttari (1995). On the  $^{207}\text{Pb}/^{204}\text{Pb}$  vs.  $^{206}\text{Pb}/^{204}\text{Pb}$  diagram (Fig. 13B) the narrow population of data points are located close to the lead isotope evolution curve of the “mantle” reservoir ( $\mu = 8.9$ ) defined by the Plumbotectonics Model 1 in Zartman

and Doe (1981). The Pb-Pb ages calculated according to this model are scattered between 1785 and 1838 Ma with the error weighted mean value at  $1818 \pm 5$  (MSWD = 2.6). These ages are slightly older than the 1760–1770 Ma ages for the rims and homogeneous/oscillatory zoned grains of xenotime from the Type 3 veins (see Ch. 4.3). The average  $\mu$  and  $\kappa$  values are 9.0 and 3.78, respectively (Electronic Material Table 8).



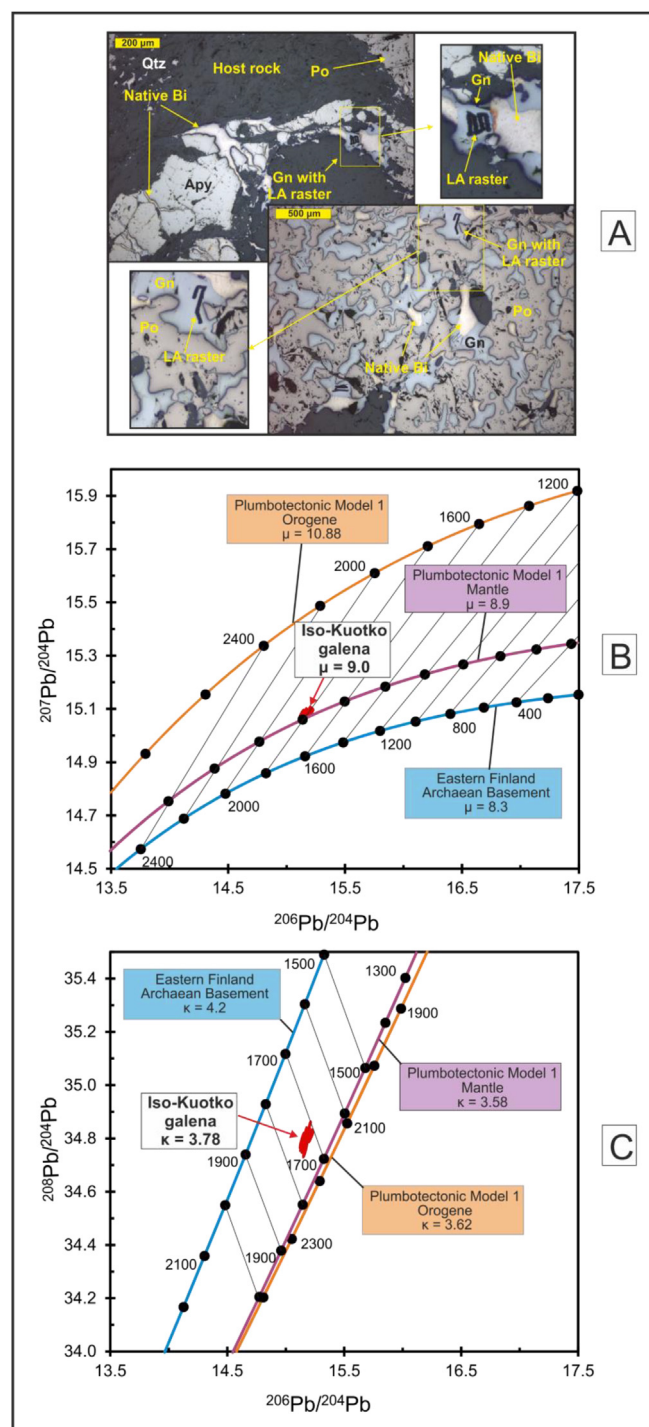


**Fig. 13.** Results of *in situ* Pb-isotope analyses in galena from the Iso-Kuotko deposit (see also [Electronic Material Table 8](#)). A – textural setting of galena grains and example of laser raster line from a LA-ICPMS analysis. B – distribution of data on the  $^{207}\text{Pb}/^{204}\text{Pb}$  vs.  $^{206}\text{Pb}/^{204}\text{Pb}$  diagram. C – distribution of data on the  $^{208}\text{Pb}/^{204}\text{Pb}$  versus  $^{206}\text{Pb}/^{204}\text{Pb}$  diagram. Pb-isotope growth curves for different reservoirs calculated according to [Zartman and Doe \(1981\)](#) single stage Plumbotectonic Model 1  $\mu$  and  $\kappa$  values for “mantle” and “orogenic” reservoirs are from [Zartman and Doe \(1981\)](#), whereas  $\mu$  and  $\kappa$  values for the Archaean basement are from [Romer \(1991\)](#).

#### 4.6. Re-Os data for arsenopyrite

Re and Os isotope analyses were completed in twelve arsenopyrite-rich sulphide samples ([Fig. 14a and b](#)) from two high grade ore zones of

the R-459 drill hole in the Kati orebody ([Fig. 2](#)). Most of the samples analysed were drilled powders of arsenopyrite (LL-958, -964, -997, -960, -1000, -961, -1001), as well as hand-picked and crushed grains of arsenopyrite (LL-1034 and LL-1035; [Table 1](#)). Drilled powders of two samples contained pyrite and chalcopyrite in addition to arsenopyrite (LL-959 and LL-999, respectively), whereas one sample (LL-998) consisted of pure chalcopyrite.

Mineralogical and textural complexities of the sulphide rich ore at Iso-Kuotko are also reflected in the Re-Os isotopic data. Results of analyses for six samples are presented by grey numbers in the [Table 1](#). These samples have almost no Os (e.g. Os concentrations are much less than 0.05 ppb) and their Re concentrations are also very low (from 0.034 to 0.916 ppb). Two arsenopyrite (LL-960 and LL-1000) samples and all of the samples containing other sulphide minerals with or without arsenopyrite belong to this group. The Re and/or Os blank contributions are higher than 1% in these samples and their data are no longer discussed.

Re and Os concentrations for the rest of the arsenopyrite samples range from 1.808 to 6.507 ppb and from 0.057 to 0.1641 ppb, respectively, with  $^{187}\text{Re}/^{188}\text{Os} = 375\text{--}746$  and  $^{187}\text{Os}/^{188}\text{Os} = 11.2\text{--}25.1$  (full details in [Table 1](#)). However, data points of these samples are scattered on the  $^{187}\text{Re}/^{188}\text{Os}$  versus  $^{187}\text{Os}/^{188}\text{Os}$  diagram and do not define an isochron ([Fig. 14C](#)). A Model 2 regression ([Ludwig, 2012](#)) yields a very imprecise age of  $1715 \pm 570$  Ma (MSWD = 863, initial  $^{187}\text{Os}/^{188}\text{Os} = 1.3$ ). Omitting two analytical runs (LL-958 and LL-997; [Table 1](#)) with the lowest Os contents in this sample group, the remaining four points form a well-defined co-linear array, but the obtained age of  $1584 \pm 18$  Ma (MSWD = 1.4, initial  $^{187}\text{Os}/^{188}\text{Os} = 3.38 \pm 0.15$ ) is geologically meaningless according to our current knowledge on hydrothermal processes in the CLGB.

## 5. Discussion

### 5.1. Interpretation of age data and radiogenic isotope compositions

#### 5.1.1. U-Pb data

Most of the individual analytical spots in zircon, monazite and xenotime from the Iso-Kuotko deposit provided concordant U-Pb data by setting the limit of acceptable concordance between 95 and 105%. Setting of this limit is arbitrary: different laboratories use discordancy filter between 1 and 30% depending on the analytical methods, data processing techniques and the nature of the geological problem under study. However, even using this data filtering method, the concordant data for individual spots do not define a concordia age in some heterogeneous monazite and xenotime cores and grains ([Fig. 6D and 9D](#)). The inconsistency of concordant data from the same type of grains/zones probably reflect the effect of alteration during superimposed hydrothermal events, as well as involvement of un-identified inclusions or mixed core-rim areas in the ablated volume of crystals, or combinations of these factors.

Petrographic observations suggest that monazite formed early in the hydrothermal mineral paragenesis at Iso-Kuotko. Textures from monazite of Type 1 veins (sample 22051503F) imply that the core of monazite likely formed synchronously with pyrite as idiomorphic inclusions of pyrite are found in it ([Figs. 5B and 6C](#)). Fracture-related and patchy compositional heterogeneity in the core of monazite could indicate dissolution – re-precipitation during later fluid flow ([Hetherington and Harlov, 2008; Poitrasson et al., 2000](#)). [Seydoux-Guillaume et al. \(2012\)](#) and [Williams et al. \(2001\)](#) found that monazite can alter and alteration can effectively disturb its  $^{238}\text{U}$ - $^{206}\text{Pb}$  system when interacting even with moderately high temperature ( $< 320^\circ\text{C}$ ) fluids. Accordingly, the heterogeneous-altered nature of monazite cores at Iso-Kuotko prevented calculation of precise U-Pb ages ([Electronic Material Table 2](#)). The monazite rims have significantly higher total REE content than the altered and inclusion bearing cores ([Fig. 7](#)) suggesting that they were deposited from different pulses of fluid flow

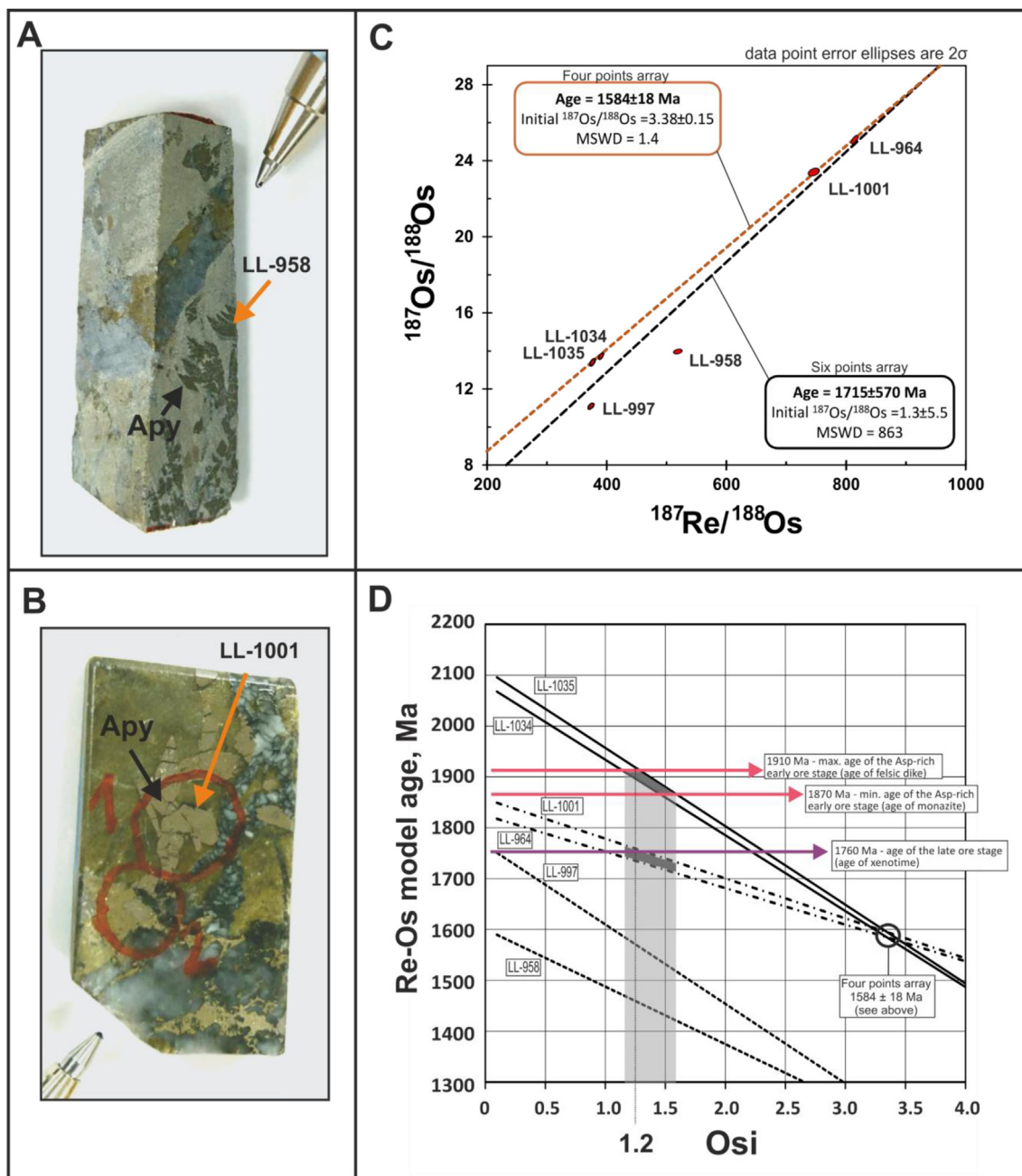


**Fig. 14.** Examples of occurrences of arsenopyrite in cores from the R-459 drill hole at the Iso-Kuotko deposit (see also Fig. 1 C), and diagrammatic presentation of results of Re-Os analyses. A and B – euhedral arsenopyrite crystals sampled for Re-Os analyses from 30.10 to 30.23 m (A) and 95.0–95.13 m (B). C – calculated Re-Os ages on the basis of co-linear data arrays for six (black dashed line) and four (red dashed line) samples. D – calculated Re-Os model ages as a function of initial  $^{187}\text{Os}/^{188}\text{Os}$  isotope ratios in the arsenopyrite samples. Additional explanations in the text. (For interpretation of the references to colour in this figure legend, the reader is referred to the web version of this article.)

during the formation of Type 1 veins. The  $^{238}\text{U}$ - $^{206}\text{Pb}$  system in the oscillatory zoned monazite rims appears to be undisturbed, as seen from the concordant data (Electronic Material Table 5). Therefore, the  $1868 \pm 15 \text{ Ma}$   $^{207}\text{Pb}/^{206}\text{Pb}$  age of the rim is considered as the minimum age for the formation of Type 1 veins.

Texture suggests that some of Type 2 veins were formed by re-activation of Type 1 veins as quartz replaces earlier formed Fe-Mg-rich carbonates, arsenopyrite and pyrite in these veins (Fig. 3K), whereas some Type 3 veins were also formed by re-opening of Type 1 and Type 2 veins as pyrrhotite partially replaces the earlier formed sulphide minerals and quartz of those veins (Fig. 3J and L). Type C xenotime grains with homogeneous compositions or faint oscillatory growth zoning in Type 3 veins, as well as similar rims around irregularly heterogeneous

cores of Type A xenotime grains in Type 2 veins unanimously show mean  $^{207}\text{Pb}/^{206}\text{Pb}$  ages at between 1760 and 1770 Ma (Figs. 8–10; Table 2). However, heterogeneous cores of Type A xenotime grains in the quartz-hosted xenotime of Type 2 veins show an older,  $1831 \pm 12 \text{ Ma}$  mean  $^{207}\text{Pb}/^{206}\text{Pb}$  age (Fig. 8), whereas the heterogeneous-patchy and resorbed Type B xenotime inclusions in pyrrhotite of Type 3 veins provided  $1859 \pm 13 \text{ Ma}$  mean  $^{207}\text{Pb}/^{206}\text{Pb}$  age (Fig. 9). This latter age is essentially the same as the age of monazite rims (e.g.  $1868 \pm 15 \text{ Ma}$ ) in Type 1 veins (Table 2).

Studies of xenotime alteration and effect of alteration on U-Pb dating of xenotime are limited but show that dissolution-re-precipitation reactions between xenotime and hydrothermal fluids depend on fluid temperature, salinity and pH (Hetherington and Harlov, 2008;

**Table 1**

Results of Re-Os isotope analyses of arsenopyrite and other sulphide separates from drill hole R-459 (Fig. 1C; Tiira orebody). Numbers with grey colour are data for samples with very low Re and Os concentrations and high blank contributions (numbers highlighted by light grey background); these data are not considered for further evaluation. Data highlighted in dark gray background are used for evaluation, only. Sulphide separates were equilibrated with single Re and Os spikes using inverse aqua regia in a sealed Carius tube; isotopic ratios measured by NTIMS on a Triton at the AIRIE Program, Colorado State University. All sulphide separates were drilled under a binocular microscope and are visually pure (or mixed, as noted) to the extent of evaluation at binocular magnification. All reported data are blank-corrected and at the two-sigma level of uncertainty; upper case letters denote different mineral separates acquired from the same sample. LL-1034 and LL-1035 comprise hand-picked grains, whereas all others were acquired with a small hand-held drill. Analyses from hand-picked grains are in good agreement, perhaps suggesting that drilled separates may have unknowingly included material of several generations. Model ages calculated for an Os initial ratio = 1.2; note that the calculated age is highly dependent on assumption of the Os initial ratio (see text and Fig. 14 for more explanation). Blank – Re = 1.04 ± 0.08 pg, Os = 0.338 ± 0.010 pg with 187Os/188Os = 0.275 ± 0.011. ASP – arsenopyrite; Cp – chalcopyrite, Py – pyrite.

AIRIE Run #	Drill Core R-459	Re (ppb)	Re Error, Abs	Os (ppb)	Os Error, Abs	<sup>187</sup> Re/ <sup>188</sup> Os	Error, Abs	<sup>187</sup> Os/ <sup>188</sup> Os	Error, Abs	rho	Model Age, Ma (Os initial = 1.2)	Error, Ma	Re Blank Contribution	Os Blank Contribution	Sample Weight (g)
LL-958	30.10-30.23m, Asp (A)	2.684	0.021	0.0702	0.0004	518.1	6.1	14.003	0.107	0.321	1465.3	26.9	0.1%	1.0%	0.4786
LL-964	30.10-30.23m, Asp (B)	6.507	0.011	0.1641	0.0011	814.2	4.5	25.130	0.183	0.644	1738.8	22.6	0.0%	0.4%	0.4985
LL-997	30.10-30.23m, Asp (C)	1.808	0.005	0.0568	0.0003	374.8	2.4	11.189	0.079	0.553	1578.6	27.1	0.4%	0.5%	0.4135
LL-998	30.10-30.23m, Cp (D)	0.916	0.011	0.0144	0.0001	500.0	8.4	4.977	0.038	0.239	-	-	0.9%	1.8%	0.4268
LL-1034	30.10-30.23m, Asp (E)	2.053	0.004	0.0704	0.0004	391.7	2.2	13.825	0.095	0.615	1903.9	29.0	0.1%	0.6%	0.5073
LL-1035	30.10-30.23m, Asp (F)	2.283	0.005	0.0800	0.0004	377.9	2.1	13.524	0.090	0.598	1926.3	29.5	0.1%	0.6%	0.5150
LL-959	84.95-85.10m, Asp-Py (A)	0.153	0.040	0.0021	0.0001	1707.9	625.1	30.004	2.110	0.168	-	-	1.2%	22.2%	0.5511
LL-999	84.95-85.10m, Asp-Cp (B)	0.034	0.002	0.0014	0.0000	320.8	23.3	13.196	0.377	0.351	-	-	13.3%	11.3%	0.6449
LL-960	85.50-85.70m, Asp (A)	0.564	0.008	0.0080	0.0003	4231.9	173.8	87.867	3.340	0.824	-	-	0.4%	7.4%	0.5237
LL-1000	85.50-85.70m, Asp (B)	0.581	0.003	0.0109	0.0005	6896.4	299.5	198.677	8.785	0.962	-	-	1.2%	2.1%	0.4917
LL-961	95.00-95.13m, Asp (A)	0.140	0.047	0.0019	0.0001	960.2	442.3	13.508	0.642	0.084	-	-	1.7%	28.3%	0.4369
LL-1001	95.00-95.13m, Asp (B)	5.467	0.035	0.1427	0.0009	745.7	7.5	23.425	0.164	0.351	1762.8	27.2	0.1%	0.2%	0.4124
		Re > 1 ppb		Os > 0.05 ppb									Re and/or Os blank contribution unacceptable		

Hetherington et al., 2010; Hetherington et al., 2008). Specifically, xenotime has higher solubility in alkali-bearing fluids, deficient of acidic anions (e.g. F<sup>-</sup>, Cl<sup>-</sup>, CO<sub>3</sub><sup>2-</sup>; Harlov and Wirth, 2012; Hetherington et al., 2010); however, under acidic conditions xenotime will be more soluble at low pH at a given temperature (Gysi et al., 2015). Alteration products, including uraninite and thorite, can then precipitate sub-parallel to a- and c-crystallographic axes, following “fluid-aided redistribution” of U, Th and Si, potentially leaving unaltered orthogonal domains of xenotime (Hetherington and Harlov, 2008). This kind of alteration

explains the observed compositional heterogeneity in the Type B irregularly shaped xenotime inclusions in pyrrhotite and cores of Type A xenotime in quartz and the partial overlap of their compositions with the much younger rims and homogeneous-euhedral grains from the same textural settings (Fig. 11A and B). This also implies that the late fluid flow events between 1760 and 1770 Ma were incapable of pervasive dissolution – re-precipitation reactions of older xenotime grains, allowing only minor, nano-scale alteration and isolated resetting of the U-Pb system in certain crystallographic domains. Therefore irregular-

**Table 2**

Summary of results of U-Pb dating of rock-forming zircon and hydrothermal monazite and xenotime, and model Pb-Pb and model Re-Os model ages calculated from the results of Pb-isotope studies in galena and Re-Os isotope analyses in arsenopyrite from the Iso-Kutoko gold deposit. \* – felsic dike sample from the Suurikuusikko deposit; \*\* – upper intercept concordia age based on anchored line fit on U-Pb data.

Type of host unit	Mineral	Dated areas/grains	Concordia age Ma	<sup>207</sup> Pb/ <sup>206</sup> Pb age Ma	Re-Os model age Ma
Felsic porphyry dyke	Zircon	Homogeneous cores	1912.9 ± 3.6 n = 15, MSWD = 4.8	1913.5 ± 3.5 n = 15, MSWD = 0.8	-
Felsic porphyry dike*	Zircon	Homogenous areas in zoned magmatic zircon grains (data for inherited zircon grains are not tabulated here)	1917.0 ± 4.0 n = 6, MSWD = 1.8	1916.3 ± 6.6 n = 6, MSWD = 2.3	-
Type 1 veins	Monazite	Heterogeneous-patchy core with inclusions	-	-	-
Type 1 veins	Arsenopyrite	Rim with oscillatory zoning Fractured grains, partly replaced by sulphides and carbonates	1864.4 ± 9.1 n = 10, MSWD = 1.09	1868 ± 15 n = 10, MSWD = 1.5	1926–1904 1763–1739 1579–1465 <sup>187</sup> Os/ <sup>188</sup> Os <sub>i</sub> = 1.2
Type 2 veins	Xenotime in quartz	Type A grains, heterogeneous cores	1826.3 ± 9.0 n = 14, MSWD = 1.9	1831 ± 12 n = 14, MSWD = 2.3	-
		Type A grains, rims	1751.8 ± 8.1 n = 17, MSWD = 1.8	1761.1 ± 8.6 n = 17, MSWD = 1.4	-
Type 3 veins	Xenotime in pyrrhotite	Type B heterogeneous grains	1855 ± 13** n = 15, MSWD = 2.9	1859 ± 13 n = 10, MSWD = 2.1	-
		Type C homogeneous grains and grains with faint oscillatory zoning	1759.8 ± 6.1 n = 27, MSWD = 1.2	1769.9 ± 6.6 n = 27, MSWD = 0.99	-
Type 3 veins	Xenotime in carbonate	Type D grains with oscillatory zoning	1751.1 ± 8.3 n = 18, MSWD = 1.7	1761.6 ± 9 n = 16, MSWD = 1.17	-
Type 3 veins	Galena in pyrrhotite	Galena grains replacing pyrrhotite	-	1838–1785 μ = 8.94–9.04 κ = 3.75–3.81	-

patchy, compositionally heterogeneous xenotime, occurring as inclusions in pyrrhotite of Type 3 veins and showing slightly disturbed U-Pb system (Fig. 9D) are considered as inherited and altered xenotime that formed during an earlier stage of vein opening. The 1859 Ma age for this kind of xenotime in Type 3 veins confirms the minimum 1860–1870 Ma for formation of the earliest, Type 1 veins. The heterogeneous cores of Type A xenotime in the Type 2 barren quartz veins could also be inherited from Type 1 veins and thus the c. 1830 Ma age can be interpreted as an apparent minimum age due to alteration or ablation of mixed core-rim volumes. However, the largely consistent and concordant U-Pb data indicate that the potential re-distribution of U and Pb contents within the grains due to the overprinting hydrothermal events did not significantly disturb the overall U-Pb system in these cores. Thus the obtained 1830 Ma U-Pb age may also indicate an age for opening up of Type 2 veins and the 1761 Ma mean  $^{207}\text{Pb}/^{206}\text{Pb}$  age of the rims reflects their further opening during the late hydrothermal events.

### 5.1.2. Pb-isotope data for galena

The very narrow ranges of Pb isotope ratios of galena occurring in the late stage fractures together with native gold and bismuth minerals suggest crystallization from a single fluid of homogeneous Pb isotope composition. The model ages of galena are between 1785 and 1838 Ma (Electronic Material Table 8) with a weighted mean value of  $1818 \pm 5$ , slightly older than the U-Pb ages for xenotime (1760–1770 Ma) from the same mineralization stage. The average  $\mu = 9.0$  value for galena apparently indicates a mantle source of uranogenic lead (Fig. 13C). However, the  $\kappa$  values spreading from 3.75 to 3.81 are inconsistent with this model and suggest involvement of a source with depleted uranogenic and enriched thorogenic lead in relation to the 1.7–1.8 Ga mantle. This points towards a “lower crust” source region ( $\kappa = 5.94$ ) according to the Plumbotectonic Models in Zartman and Doe (1981). On the basis of the results of a regional scale lead isotope studies in ore deposits in Finland, Vaasjoki (1981), Huhma (1986) and Huhma et al. (2012) concluded that the Archaean basement source (e.g. lower crust) had a significant effect on the lead-isotope ratios of galena in Paleoproterozoic ore deposits. Heilimo et al. (2009) reported low initial lead isotope compositions for the 1.77 Ga Nattanen granite, which also has very low initial Nd isotope ratio (Huhma, 1986) and thus clearly indicating lower crust origin. Romer (1991) has also shown that the Archaean basement in Eastern Finland has “lower crust” type lead isotope composition with  $\mu$  values between 8.0 and 8.3 and  $\kappa$  values at around 4.2 (Fig. 13B and C). Thus the Pb isotope ratios of galena from the Iso-Kuotko deposit most probably reflect mixed mantle and Archaean basement sources of lead. Mass transfer between the crust and mantle along the Kiistala Shear Zone at approximately the same time as the age of late stage ore forming processes is also indicated by the presence of lamprophyre dikes with a  $1718 \pm 9$  Ma Rb-Sr isochron age (Mänttari, 1998) in the Iso-Kuotko deposit. This Rb-Sr age is mostly based on biotite and thus it can be interpreted as the minimum age of dike emplacement and mineralization.

### 5.1.3. Re-Os data for arsenopyrite

The open-system behaviour of the Re-Os isotope system in arsenopyrite and other sulphides during metamorphism and overprinting fluid flow events was demonstrated by Stein et al. (2007), Coggon et al. (2015) and Saintilan et al. (2017). Especially, mildly oxidizing hydrothermal fluids may have an important effect on the Re-Os isotope systems in sulphide minerals (Stein, 2014). Therefore the scattering of Re-Os data for arsenopyrite at Iso-Kuotko on the Fig. 14C is most probably the result of Re and Os mobilization and re-setting of the Re-Os isotope system during the late-stage hydrothermal processes which overprinted the early stage, arsenopyrite rich refractory gold ore.

Re-Os data from the Iso-Kuotko show some internal consistencies when the mineralogy and texture of the ore, as well as the results of U-Pb dating, are also taken into consideration. Ore textures suggest that

arsenopyrite was deposited earlier than the ~1870 Ma old monazite and xenotime in the veins, whereas the ~1910 Ma age for rock-forming zircon from a felsic dike constrains the oldest possible age of the mineralization. Two hand-picked arsenopyrite grains (LL-1034 and LL-1035, Table 1) from the same sample provided consistent Re-Os isotope ratios thus it is reasonable to assume that the Re-Os system is the least disturbed in these grains. Fig. 14D shows the possible Re-Os model ages for these grains as a function of initial Os-isotope ratios. Considering the 1.91 Ga maximum possible ages for arsenopyrite, the initial  $^{187}\text{Os}/^{188}\text{Os}$  isotope ratio ( $\text{Os}_i$ ) can be fixed at 1.2. Taking into account the 1.87 minimum age of arsenopyrite, the initial Os isotope ratio is around 1.5. The possible model ages for the rest of the arsenopyrite samples do not reach the 1.91–1.87 Ga range unless extremely negative  $\text{Os}_i$  values are considered (Fig. 14D). However, the model ages for two separates with the most radiogenic Re-Os isotope compositions (LL-964 and LL-1001, Table 1) are from 1763 to 1717 Ma when  $\text{Os}_i$  values from 1.2 to 1.5 considered. These model ages are in good agreement with the 1770–1760 Ma U-Pb ages for xenotime from the late stage ore. Thus the Re-Os model ages for these latter samples suggest that some parts of arsenopyrite were recrystallized during the 1760–1770 Ma hydrothermal event and the Re-Os clock was disturbed in those domains/grains. This is consistent with the texture of arsenopyrite grains showing partial replacement by late stage native bismuth/gold and pyrrhotite bearing mineral assemblages (Fig. 3I and J). According to this model, and even considering the *in situ* growth of radiogenic  $^{188}\text{Os}$  between 1.91 and 1.77 Ga, the initial  $^{187}\text{Os}/^{188}\text{Os}$  ratios were not significantly different during the early and late stage mineralization, suggesting the same crustal source of fluids during the deposition of the early and late stage ores.

The Re-Os model ages for the arsenopyrite separates with the very low Os-content (LL-958 and LL1001) are much less than 1770–1760 Ma for any positive initial Os isotope ratios (Fig. 14D). Results of Pb-isotope studies on sulphides from the Iso-Kuotko deposit by Mänttari (1995) permits the hypothesis of a hydrothermal overprint on the Paleoproterozoic mineralization by mobilization of oxidative basin fluids at c. 400 Ma, during the Caledonian orogeny. The apparently “young”, ~1500 Ma Re-Os model ages for some arsenopyrite samples (Table 1) may reflect the effect of a similar overprint during the post-Svecofennian exhumation of the basement but the available data do not allow further refinement of this model.

### 5.2. Implications of results for orogenic gold metallogeny and tectonic evolution in the CLGB

The  $^{207}\text{Pb}/^{206}\text{Pb}$  age of  $1914 \pm 4$  Ma for the Iso-Kuotko felsic porphyry host rock is within error of ages for other felsic intrusions in the Kittilä region, including the felsic dike from the Suurikuusikko deposit ( $1916 \pm 7$  Ma, this study), the Ruoppapalo tonalite-diorite pluton ( $1914 \pm 3$ , Rastas et al., 2001 and  $1905 \pm 5$  Ma; Ahtonen et al., 2007) ~3 km east and north of Iso-Kuotko (Fig. 1a) and the N-S-trending Nyssäkoski dike ( $1919 \pm 8$  Ma) ~10 km SW of Iso-Kuotko (not shown in Fig. 1). These intrusions are reportedly syntectonic and record obduction of the Kittilä Group (Hanski and Huhma, 2005; Rastas et al., 2001). Their age of emplacement fits into the 1.92–1.88 Ga time-interval of microcontinent and arc accretion during the Svecofennian orogeny (Fig. 15; Korja et al., 2006). Intrusion of felsic dikes along the KiSZ may suggest syntectonic magma emplacement during wrench-dominated N-S shearing (McFadden et al., 2010), marking the first recognisable period of tectonism along the KiSZ and thus corresponds to the age of the D1-D2 ductile deformation (Fig. 15). Consistency with age data for the Ruoppapalo granite and Nyssäkoski felsic dikes implies N-S shearing was not isolated to the KiSZ but widespread, causing regional tectonomagmatic activity. Re-Os dating of arsenopyrite from Suurikuusikko produced an age of  $1916 \pm 19$  Ma (Wyche et al., 2015), concurrent with the above mentioned magmatic activity (Fig. 15). Although textural evidence linking magmatism to the Au–As-rich

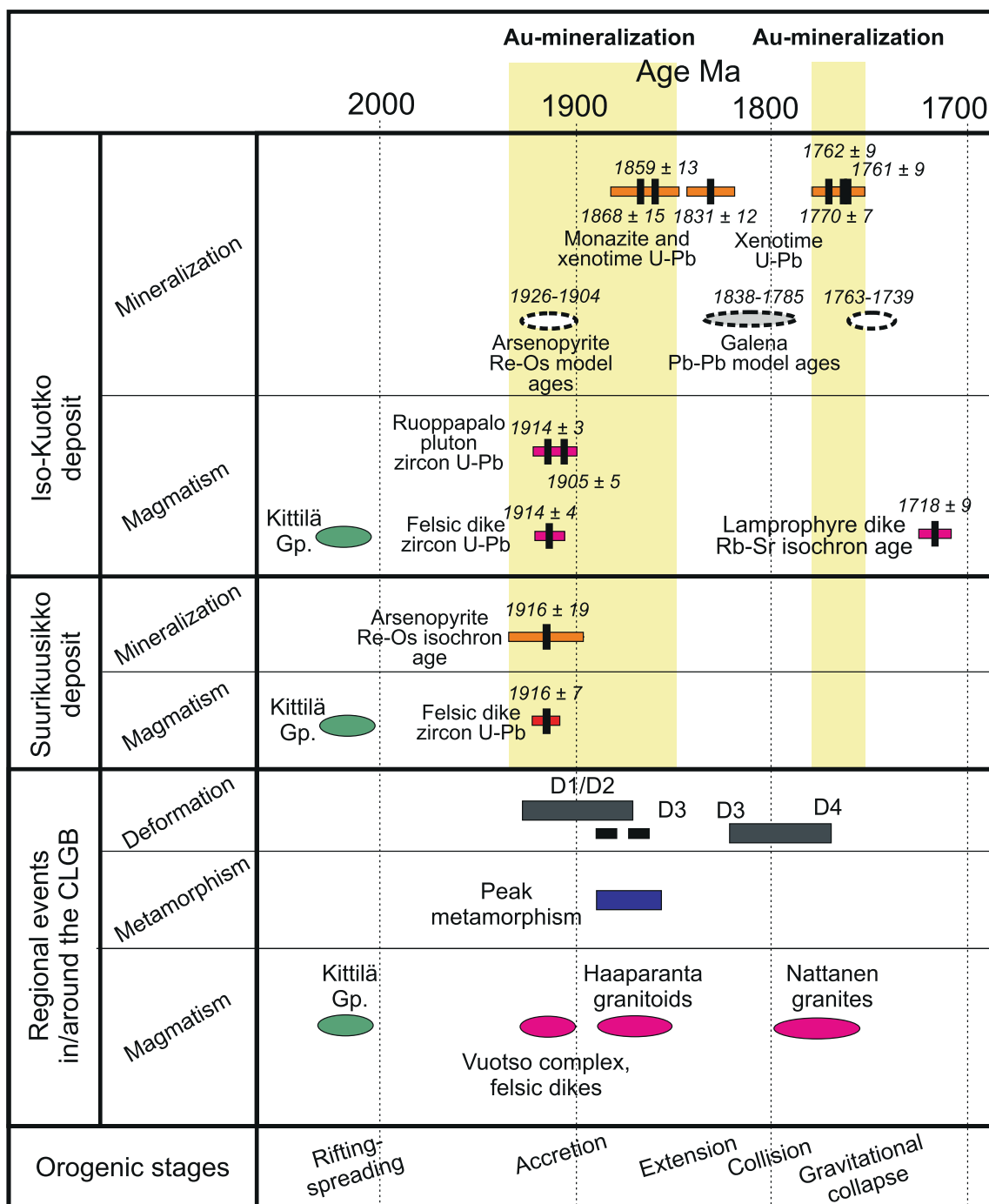


**Fig. 15.** Summary of geochronological data for the Iso-Kuotko and Suurikuusikko gold deposits, and ages for magmatism, metamorphism and deformation events in the Central Lapland Greenstone belt in the framework of the Svecofennian orogeny. Sources of literature data in this diagram are referred to in the text.

mineralization is yet to be found, cogenesis of these processes seems plausible and has been recognised at numerous Au deposits globally (Hall and Wall, 2007; Hart et al., 2002).

Our observations suggest that the minimum age for the first stage of hydrothermal events responsible for extensive quartz + carbonate-(albite) veining with refractory gold in arsenopyrite and pyrite is 1860–1870 Ma at the Iso-Kuotko deposit (Fig. 15). Interpretation of Re-Os data from arsenopyrite is also consistent with this minimum age of early stage mineralization. Numerous ages of c.1.89–1.86 Ga for the synorogenic granitoids of the Haaparanta suite are found along the western boundary of the CLGB, along the Pajala Shear Zone on the Swedish–Finnish border (Fig. 1a; Väänänen and Lehtonen, 2001;

Bergman et al., 2006 and references therein; Niiranen, 2005; Lahtinen et al., 2015b), as well as north of the Iso-Kuotko deposit (Fig. 1A). Some intrusions in the Central Lapland Granite Complex (approx. 50 km to the south of the Sirkka Line) also have similar ages (Ahtonen et al., 2007). Lahtinen et al. (2015a) tentatively proposed that this age represents a period of peak metamorphism in the CLGB with associated magmatism during extension, which followed accretion and buckling at 1880–1860 Ma. Consistency of previous age data with xenotime and monazite in this study may suggest transmission of stress to mechanically-weakened crust on the KiSZ during the final stages of accretion – buckling (Armitage and Allen, 2010; Lahtinen et al., 2015a). Tectono-thermal perturbations could increase the hydraulic gradient along

major fault zones in a thrust and fold belt, allowing an influx of fluid that may result in extensive alteration and mineralization (Kyser, 2007; Middleton et al., 2014). A similar process may have led to the formation of the Type 1 veins at the Iso-Kuotko deposit. Because Type 1 veins cut crenulated foliation of the host rock, their formation can be connected to the hydrothermal processes between D1/D2 and D3 brittle-ductile deformation stage (Fig. 15).

Xenotime cores dated at c. 1830 in Type 2 veins at the Iso-Kuotko deposit most likely records localised re-opening of Type 1 veins. Tectonic events at around 1820 Ma correspond to a transient extension stage followed the accretion and buckling before the final continental collision stage of the Svecofennian orogeny (Lahtinen et al., 2005; Lahtinen et al., 2015a). The formation of the pyrrhotite rich vein-breccia ore (Type 3 veins), which includes the major stage of visible gold mineralization between 1760 and 1770 Ma is temporally coincident with the spatially expansive 1800–1765 Ma post-orogenic granitic magmatism (Nattanen type granites; Figs. 1 and 15) extending from the Norbotten region of northern Sweden to Murmansk, Russia (Corfu and Evins, 2002; Lahtinen et al., 2005; Nironen, 2005) and corresponds to the c. 1.77 Ga D4 deformation stage of the tectonic evolution in the CLGB. Widespread crustal melting likely derives from decompression or relaxation-related melting during gravitational collapse, following cessation of Svecofennian orogenesis (Lahtinen et al., 2005; Korja et al., 2006; Nironen, 2005). The approximately 150 Ma of orogenesis caused substantial shortening and thickening of the Svecofennian crustal domain (Lahtinen and Huhma, 1997; Nironen, 1997). This would provide an excess in gravitational potential to drive extension, while an elevated geothermal gradient caused extensive melting and regional thermal perturbations (Liu, 2001). Periods of extension and increased thermal activity then likely drove metal-laden fluids along highly permeable, crustal-scale reactivated shear zones, such as the KiSZ causing localised mineralization. Occurrences of post-peak metamorphic, gold-bearing quartz–carbonate veins of similar orientation (N–S), are also known along the Hanhimaa Shear Zone (HaSZ 10 km to west of Iso-Kuotko; Fig. 1A) with similar orientation to KiSZ (Saalman and Niiranen, 2010). Evidence of regional fluid flow and mineralization with similar age is also known 50 km SW at the Saattopora Cu–Au deposit along the SiSZ (Fig. 1A) where monazite and uraninite bearing pyrobitumen in the quartz–carbonate–sulphide–Au veins are dated at  $1784 \pm 11$  and  $1781 \pm 18$  Ma, respectively (U–Pb data by TIMS in Mänttari, 1995).

## 6. Conclusions

The current study provides a comprehensive geochronological dataset of hydrothermal processes along the Kiistala Shear Zone in the northern part of the CLGB. The new U–Pb age data for magmatic zircon as well as hydrothermal monazite and xenotime together with the earlier published geochronological data for magmatism and hydrothermal ore deposition support distinction of at least three periods of tectonothermal activity with two stages of Au mineralization during the c. 150 Ma long evolution of the Svecofennian orogeny in the CLGB (Fig. 15).

Zircon separates from the felsic porphyry host rocks of gold mineralization at Iso-Kuotko and Suurikuusikko gave ages at 1914–1916 Ma and thus emplacement of these dikes can be related to syntectonic magmatism during wrench-dominated shearing that also induced Au-rich arsenopyrite–pyrite mineralization (~1916 Ma) at Suurikuusikko. The minimum age of auriferous sulphide (refractory gold) mineralization, as it is recorded by vein-hosted hydrothermal monazite and xenotime is between 1860 and 1870 Ma at Iso-Kuotko. Model calculations based on Re–Os data obtained from arsenopyrite permit that the early stage refractory gold mineralization at Iso-Kuotko could be as old as the similar arsenopyrite rich gold ore at Suurikuusikko. Such fluid flow and local thermal perturbations were most likely driven by transmission of far-field stress to mechanically

weakened crust during the accretional stage (D1/D2–D3 deformation stages) of the Svecofennian orogenesis.

A second and third generation of hydrothermal xenotime, dated at 1830 Ma, as well as 1760–1770 Ma, was also identified in tandem with detailed petrography and EPMA and indicate repeated re-activation of the Kiistala Shear Zone at the Iso-Kuotko deposit. The repeated hydrothermal activity along the same structures resulted in disturbance of the Re–Os isotope system in some grains or domains of auriferous arsenopyrite from the early stage mineralization. The 1760–1770 Ga age for hydrothermal minerals represents the main ore-forming stage, which produced visible gold mineralization in sulphide-native bismuth bearing veins and breccias at Iso-Kuotko. The post-orogenic crustal-scale fluid circulation was most probably driven by an elevated geothermal gradient during post-orogenic gravitational collapse. Lead isotope studies implicate both mantle and lower crust of metal sources.

Constraining ages for fluid flow and mineralization on the KiSZ, this work contributes vital information for better understanding the tectonic evolution of the CLGB. The obtained precise ages for multiple gold deposition events along the KiSZ will further refine exploration models in the CLGB and provide a basis for use of structural data in regional-scale evaluation of mineral prospectivity. This study also confirms the use of hydrothermal monazite and xenotime as robust geochronological tools with capacities to distinguish multiple hydrothermal events by *in situ* U–Pb dating by LA-ICPMS in single crystals.

## Acknowledgments

The authors are grateful to Jyrki Korteniemi and Jukka Välimaa (Agnico-Eagle Oy, Kittilä Mine, Finland) for allowing access to drill-cores and geochemical data. Tom Andersen (University of Oslo) is greatly acknowledged for providing the software used for U–Pb data reduction. Ferenc Molnár, Jr. (University of Notre Dame) is thanked for development of Excel worksheets for performing model calculations in the Pb–Pb and Re–Os isotope systems. This work was supported by the Academy of Finland No. 281670 “Mineral systems and mineral prospectivity in Finnish Lapland” project and is a SGL (Finnish Geosciences Research Laboratory) contribution. Reviewers are thanked for their insightful comments, which highly supported the improvement of the final version of the manuscript.

## Appendix A. Supplementary data

Supplementary data associated with this article can be found, in the online version, at <https://doi.org/10.1016/j.oregeorev.2018.08.015>.

## References

- Ahtonen, N., Hölta, P., Huhma, H., 2007. Intracratonic Palaeoproterozoic granitoids in northern Finland: prolonged and episodic crustal melting events revealed by Nd isotopes and U–Pb ages on zircon. *Bull. Geol. Soc. Finland* 79, 143–174.
- Agnico Eagle, 2015. Annual Report. [http://s1.q4cdn.com/150142668/files/doc\\_financials/2015/2015-Annual-Report.pdf](http://s1.q4cdn.com/150142668/files/doc_financials/2015/2015-Annual-Report.pdf).
- Armitage, J.J., Allen, P.A., 2010. Cratonic basins and the long-term subsidence history of continental interiors. *J. Geol. Soc. London* 167, 61–70.
- Bergman, S., Billström, K., Persson, P.-O., Skiöld, T., Evins, P., 2006. U–Pb age evidence for repeated Palaeoproterozoic metamorphism and deformation near the Pajalashear zone in the northern Fennoscandian shield. *GFF* 128, 7–20.
- Carpenter, R.L., Duke, N.A., Sandeman, H.A., Stern, R., 2005. Relative and absolute timing of gold mineralization along the Meliadine trend, Nunavut, Canada: evidence for Palaeoproterozoic gold hosted in an Archean greenstone belt. *Econ. Geol.* 100, 567–576.
- Cherniak, D.J., 2006. Pb and rare earth element diffusion in xenotime. *Lithos* 88, 1–14.
- Cherniak, D.J., Watson, E.B., Grove, M., Harrison, T.M., 2004. Pb diffusion in monazite: a progress report on a combined RBS/SIMS study. *Geochim. Cosmochim. Acta* 68, 829–840.
- Coggon, J.A., Luguét, A., Fonseca, R.O.C., Lorand, J.-P., Heuser, A., Appel, P.W.U., 2015. Understanding Re–Os systematics and model ages in metamorphosed Archean ultramafic rocks: a single mineral to whole-rock investigation. *Geochim. Cosmochim. Acta* 167, 205–240.
- Corfu, F., Evins, P.M., 2002. Late Palaeoproterozoic monazite and titanite U–Pb ages in the Archean Suomijärvi Complex, N-Finland. *Precamb. Res.* 116, 171–181.

- Daly, J.S., Balagansky, V.V., Timmerman, M.J., Whitehouse, M.J., de Jong, K., Guise, P., Bogdanova, S., Gorbatshev, R., Bridgwater, D., 2001. Ion microprobe U-Pb zircon geochronology and isotopic evidence for a trans-crustal suture in the Lapland-Kola Orogen, northern Fennoscandian Shield. *Precamb. Res.* 105, 289–314.
- Eilu, P., 2015. Overview on gold deposits in Finland. In: Maier, W.D., Lahtinen, R., O'Brien, H. (Eds.), *Mineral deposits of Finland*. Elsevier, Amsterdam, pp. 377–410.
- Eilu, P., Pankka, H., Keinänen, V., Kortelainen, V., Niiranen, T., Pulkkinen, E., 2007. Characteristics of gold mineralisation in the greenstone belts of northern Finland. *Geol. Surv. Finland Spec. Pap.* 44, 57–106.
- Eilu, P. and Niiranen, T., 2013. Gold deposits in northern Finland. Excursion guidebook FIN1, SGA Biennial Meeting. Geological Survey of Sweden, Uppsala, pp. 12.
- Fielding, I.O.H., Johnson, S.P., Zi, J.-W., Rasmussen, B., Muhling, J.R., Dunkley, D.J., Sheppard, S., Wingate, M.T.D., Rogers, J.R., 2017. Using in situ SHRIMP monazite and xenotime geochronology to determine the age of orogenic gold mineralization: an example from the Paulsens Mine, Southern Pilbara Craton. *Econ. Geol.* 112, 1205–1230.
- Fourgrouse, D., Micklethwaite, S., Ulrich, S., Miller, J., Godel, B., Adams, D., McCuaig, T.C., 2017. Evidence for two stages of mineralization in West Africa's largest gold deposit: Obuasi, Ghana. *Econ. Geol.* 112, 3–22.
- Förster, H.-J., 2006. Composition and origin of intermediate solid solutions in the system thorite-xenotime-zircon-coffinite. *Lithos* 88, 35–55.
- Gaál, G., Berthelsen, A., Gorbatshev, R., Kesola, R., Lehtonen, M.I., Marker, M., Raase, P., 1989. Structure and composition of the Precambrian crust along the POLAR Profile in the northern Baltic Shield. *Tectonophysics* 162, 1–25.
- Gazley, M.F., Vry, J.K., Millet, M.-A., Handler, M.R., Pleiss, E., Baker, J.A., 2016. New age constraints on metamorphism, metasomatism and gold mineralisation at Plutonic Gold Mine, Marymia Inlier, Western Australia. *Aust. J. Earth Sci.* 63, 413–426.
- Goldfarb, R.J., Baker, T., Dubé, B., Groves, D.L., Hart, C.J.R., Gosselin, P., 2005. Distribution, character, and genesis of gold deposits in metamorphic terranes. *Society of Economic Geologists Economic Geology 100th Anniversary Volume*, pp. 407–450.
- Groves, D.L., Goldfarb, R.J., Robert, F., Hart, C.J.R., 2003. Gold deposits in metamorphic belts: overview of current understanding, outstanding problems, future research, and exploration significance. *Econ. Geol.* 98, 1–29.
- Groves, D.L., Santosh, M., 2016. The giant Jiadong gold province: the key to a unified model for orogenic gold deposits? *Geosci. Front.* 7, 409–417.
- Gysi, A.P., William-Jones, A.E., Hanski, E., 2015. The solubility of xenotime-(Y) and other HREE phosphates (DyPO<sub>4</sub>, ErPO<sub>4</sub> and YbPO<sub>4</sub>) in aqueous solutions from 100 to 250°C and *p*<sub>H</sub>. *Chem. Geol.* 401, 83–95.
- Hall, G., Wall, V., 2007. Geologyworks—the use of regional geological maps in exploration. In: Milereit, B. (Ed.), *Proceedings of Exploration '07: Fifth Decennial Conference on Mineral Exploration*, pp. 51–60.
- Hanski, E., Huhma, H., 2005. Central Lapland greenstone belt. In: Lehtinen, M., Nurmi, P.A., Rämö, O.T. (Eds.), *Precambrian Geology of Finland – Key to the Evolution of the Fennoscandian Shield*. Elsevier, Amsterdam, pp. 139–194.
- Harlov, D.E., Wirth, R., 2012. Experimental incorporation of Th into xenotime at middle to lower crustal P-T utilizing alkali-bearing fluids. *Am. Mineral.* 97, 641–652.
- Hart, C.J.R., McCoy, D., Goldfarb, R.J., Smith, M., Roberts, P., Hulstein, R., Bakke, A.A., Bundtzen, T.K., 2002. *Geology, exploration and discovery in the Tintina gold province, Alaska and Yukon*. Society of Economic Geologists Special Publication 9, 241–274.
- Heilimo, E., Jaana Halla, J., Lauri, L.S., Rämö, T., Huhma, H., Kurhila, M.I., Front, K., 2009. The Paleoproterozoic Nattanen-type granites in northern Finland and vicinity – a postcollisional oxidized A-type suite. *Bull. Geol. Soc. Finland* 81, 7–38.
- Hetherington, C.J., Harlov, D.E., 2008. Metasomatic thorite and uraninite inclusions in xenotime and monazite from granitic pegmatites, Hydra anorthosite massif, south-western Norway: mechanics and fluid chemistry. *Am. Mineral.* 93, 806–820.
- Hetherington, C.J., Harlov, D.E., Budzyń, B., 2010. Experimental metasomatism of monazite and xenotime: mineral stability, REE mobility and fluid composition. *Mineral. Petrol.* 99, 165–184.
- Hetherington, C.J., Jercinovic, M.J., Williams, M.L., Mahan, K., 2008. Understanding geological processes with xenotime: composition, chronology, and a protocol for electron probe microanalysis. *Chem. Geol.* 254, 133–147.
- Hölttä, P., Huhma, H., Mänttari, I., Paavola, J., 2000. P-T-t development of Archaean granulites in Varpaisjärvi, Central Finland II. Dating of high-grade metamorphism with the U-Pb and Sm-Nd methods. *Lithos* 50, 121–136.
- Huhma, H., 1986. Sm-Nd, U-Pb and Pb-Pb isotopic evidence for the origin of the Early Proterozoic Svecofennian crust in Finland. *Geol. Surv. Finland, Bull.* 337, 1–48.
- Huhma, H., Mänttari, I., Peltonen, P., Kontinen, A., Halkoaho, T., Hanski, E., Hokkanen, T., Hölttä, P., Juopperi, H., Konnunaho, J., Lahaye, Y., Luukkonen, E., Pietikäinen, K., Pulkkinen, A., Sorjonen-Ward, P., Vaasjoki, M., Whitehouse, M., 2012. The age of the Archaean greenstone belts in Finland. *Geol. Surv. Finland Spec. Pap.* 54, 74–175.
- Härkönen, I., Pankka, H., Rossi, S., 2000. Summary report: The Iso-Kuotko gold prospects, northern Finland. Geological Survey of Finland (GTK), Report No. C/M06/2744/00/1/10.
- Hölttä, P., Väisänen, M., Väänänen, J., Manninen, T., 2007. Paleoproterozoic metamorphism and deformation in Central Lapland, Finland. *Geol. Surv. Finland Spec. Pap.* 44, 7–56.
- Korja, A., Lahtinen, R., Nironen, M., 2006. The Svecofennian orogen: a collage of microcontinents and island arcs. In: Gee, D.G., Stephenson, R.A. (Eds.), *European Lithosphere Dynamics*. Geological Society, London, Memoirs, pp. 561–578.
- Kositcin, N., McNaughton, N.J., Griffin, B.J., Fletcher, I.R., Groves, D.L., Rasmussen, B., 2003. Textural and geochemical discrimination between xenotime of different origin in the Archaean Witwatersrand Basin, South Africa. *Geochim. Cosmochim. Acta* 67, 709–731.
- Kyser, K.T., 2007. Fluids, basin analysis and mineral deposits. *Geofluids* 7, 235–257.
- Lahtinen, R., 2012. Evolution of the bedrock of Finland. In: Haapala, I. (Ed.), *From the Earth's Core to Outer Space*. Springer-Verlag, Berlin/Heidelberg, pp. 47–60.
- Lahtinen, R., Huhma, H., 1997. Isotopic and geochemical constraints on the evolution of the 1.93-1.79 Ga Svecofennian crust and mantle in Finland. *Precamb. Res.* 82, 13–34.
- Lahtinen, R., Huhma, H., Lahaye, Y., Jonsson, E., Manninen, T., Lauri, L.S., Bergman, S., Hellström, F., Niiranen, T., Nironen, M., 2015b. New geochronological and Sm-Nd constraints across the Pajala shear zone of northern Fennoscandia: reactivation of a Paleoproterozoic suture. *Precamb. Res.* 256.
- Lahtinen, R., Korja, A., Nironen, M., 2005. Paleoproterozoic tectonic evolution. In: Lehtinen, M., Nurmi, P.A., Rämö, O.T. (Eds.), *Precambrian Geology of Finland: Key to the Evolution of the Fennoscandian Shield*. Elsevier, Amsterdam, pp. 481–532.
- Lahtinen, R., Sayab, M., Karell, F., 2015a. Near-orthogonal deformation successions in the poly-deformed Paleoproterozoic Martimo belt: implications for the tectonic evolution of Northern Fennoscandia. *Precamb. Res.* 270, 22–38.
- Lehtonen, M.I., Airo, M.L., Eilu, P., Hanski, E., Kortelainen, V., Lanne, E., Manninen, T., Rastas, P., Räsänen, J., Virransalo, P., 1998. Kittilän vihräkivalueen geologia. *Lapin vulkaniittiprojektin raportti*. Summary: the stratigraphy, petrology and geochemistry of the Kittilä greenstone area, northern Finland. A Report of the Lapland Volcanite Project. Geological Survey of Finland.
- Liu, M., 2001. Cenozoic extension and magmatism in the North American Cordillera: the role of gravitational collapse. *Tectonophysics* 342, 407–433.
- Ludwig, K.R., 2012. *Users Manual for ISOPLOT/EX, Version 3. A Geochronological Toolkit for Microsoft Excel*. Berkeley Geochronological Centre Special Publication.
- McCuaig, T.C., Beresford, S., Hronsky, J., 2010. Translating the mineral systems approach into an effective exploration targeting system. *Ore Geol. Rev.* 38, 128–138.
- McFadden, R.R., Teyssier, C., Suddoway, C.S., Whitney, D.L., Fanning, C.M., 2010. Oblique dilation, melt transfer, and gneiss dome emplacement. *Geology* 38, 375–378.
- Middleton, A.W., Uysal, I.T., Golding, S.D., Förster, H.-J., Allen, C.M., Feng, Y., Rhede, D., Marshall, V.J., van Zyl, J., 2014. Geochronological (U-Pb, U-Th-total Pb, Sm-Nd) and geochemical (REE, 87Sr/86Sr, δ18O, δ13C) tracing of intraplate tectonism and associated fluid flow in the Warburton Basin, Australia. *Contrib. Miner. Petrol.* 168, 1058–1060.
- Molnár, F., O'Brien, H., Stein, H., Cook, N., 2017. Geochronology of hydrothermal processes leading to the formation of the Au-U mineralization at the Rompas prospect, Peräpohja belt, northern Finland: application of paired U-Pb dating of uraninite and Re-Os dating of molybdenite to the identification of multiple hydrothermal events in a metamorphic terrane. *Minerals* 7, 171. <https://doi.org/10.3390/min7090171>.
- Molnár, F., O'Brien, H., Lahaye, Y., Käpyaho, A., Sorjonen-Ward, P., Hyodo, H., Sakellaris, G., 2016. Signatures of multiple mineralization processes in the Archaean orogenic gold deposits of the Pampalo mine, Hattu Schist Belt, Eastern Finland. *Econ. Geol.* 111, 1659–1703.
- Mutanen, T., Huhma, H., 2001. U-Pb geochronology of the Koitelainen, Akanvaara and Keivitsa layered intrusions and related rocks. In: Vaasjoki, M. (Ed.), *Radiometric age determinations from Finnish Lapland and their bearing on the timing of Precambrian volcano-sedimentary sequences*. Geological Survey of Finland, Special Paper 33, pp. 229–246.
- Müller, W., Shelley, M., Miller, P., Broude, S., 2009. Initial performance metrics of a new custom-designed ArF excimer LA-ICPMS system coupled to a two-volume laser-ablation cell. *J. Anal. At. Spectrom.* 24, 209–214.
- Mänttari, I., 1995. Lead isotope characteristics of epigenetic gold mineralization in the Paleoproterozoic Lapland greenstone belt, northern Finland. *Bulletin* 381, 70.
- Mänttari, I. (1998) Iso-Kuotkon happaman porfyyrin (A1262) ja lamprofyyriinyytteiden (R308 + R311 + A1168) isotoopitutkimukset. Unpublished Research Report #CKY/23/1998/28, Geological Survey of Finland, 4p.
- Nironen, M., 1997. The Svecofennian Orogen: a tectonic model. *Precamb. Res.* 86, 21–44.
- Nironen, M., 2005. Proterozoic orogenic granitoid rocks. In: Lehtinen, M., Nurmi, P.A., Rämö, O.T. (Eds.), *Precambrian Geology of Finland – Key to the Evolution of the Fennoscandian Shield*. Elsevier, Amsterdam, pp. 443–480.
- Nironen, M., 2017. Structural interpretation of the Peräpohja and Kuusamo belts and Central Lapland, and a tectonic model for northern Finland. *Geological Survey of Finland, Report of Investigations* 234, 53p.
- Niiranen, T., 2005. Iron oxide-copper-gold deposits in Finland: case studies from the Peräpohja schist belt and the Central Lapland greenstone belt. University of Helsinki, Publications of the Department of Geology D6, 27 p. Available at: <https://oa.doria.fi/dspace/bitstream/10024/2687/2/ironoxid.pdf>.
- Niiranen, T., Lahti, I., Nykänen, V., Karinen, T., 2014. Central Lapland Greenstone Belt 3D modeling project final report. Geological Survey of Finland, Report of Investigation 209, 78 p.
- Pajunen, M., Poutiainen, M., 1999. Paleoproterozoic prograde metasomatic-metamorphic overprint zones in Archaean tonalitic gneisses, eastern Finland. *Bull. Geol. Soc. Finland* 71, 73–132.
- Paquette, J.-L., Tiepolo, M., 2007. High resolution (5 μm) U-Th-Pb isotope dating of monazite with excimer laser ablation (ELA)-ICPMS. *Chem. Geol.* 240, 222–237.
- Patison, N.L., 2000. Structural and fluid chemical controls on gold mineralization in the Central Lapland Greenstone Belt, northern Finland. Geological Survey of Finland, Report No. M16/2001/2.
- Patison, N.L., 2007. Structural controls on gold mineralization in the central Lapland greenstone belt. In: Ojala, J.V. (Ed.), *Gold in the Central Lapland Greenstone Belt, Finland*. Geological Survey of Finland, Special Paper 44, pp. 107–122.
- Poitrasson, F., Chenery, S., Shepherd, T., 2000. Electron microprobe and LA-ICP-MS study of monazite hydrothermal alteration: implications for U-Th-Pb geochronology and nuclear ceramics. *Geochim. Cosmochim. Acta* 64, 3283–3297.
- Pouchou, J.L., Pichoir, F., 1987. In: *Basic expressions of PAP computation for quantitative EPMA*. University of Western, Ontario, pp. 249.
- Rasmussen, B., Fletcher, I.R., Muhling, J.R., 2011. Response of xenotime to prograde

- metamorphism. *Contrib. Miner. Petrol.* 162, 1259–1277.
- Rastas, P., Huhma, H., Hanski, E. and Lehtonen, M.I., 2001. U-Pb isotopic studies on the Kittilä greenstone area, central Lapland, Finland. In: Vaasjoki, M. (Ed.), Radiometric age determinations from Finnish Lapland and their bearing on the timing of Precambrian volcano-sedimentary sequences. Geological Survey of Finland, Special Paper 33, pp. 95–141.
- Robert, F., Poulsen, K.H., Cassidy K.F., Hodgson, C.J. (2005) Gold metallogeny of the Superior and Yilgarn cratons. *Economic Geology 100th Anniversary Volume*, 1001–1034.
- Romer, R.L., 1991. The Late Archean to Early Proterozoic lead isotopic evolution of the northern Baltic Shield of Norway, Sweden and Finland. *Precamb. Res.* 49, 73–95.
- Saalmann, K., Niiranen, T., 2010. Hydrothermal alteration and structural control on gold deposition in the Hanhima shear zone and western part of the Sirkka Line. Geological Survey of Finland, Report No. M19/2741/2010/58.
- Saintilan, N.J., Creaser, R.A., Bookstrom, A.A., 2017. Re-Os systematics and geochemistry of cobaltite (CoAsS) in the Idaho cobalt belt, Belt-Purcell Basin, USA: evidence for middle Mesoproterozoic sediment-hosted Co-Cu sulfide mineralization with Grenvillian and Cretaceous remobilization. *Ore Geol. Rev.* 86, 509–525.
- Schandi, E.S., Gorton, M.P., 2004. A textural and geochemical guide to the identification of hydrothermal monazite: criteria for selection of samples for dating epigenetic hydrothermal ore deposits. *Econ. Geol.* 99, 1027–1035.
- Seydoux-Guillaume, A.-M., Montel, J.-M., Bingen, B., Bosse, V., de Parseval, P., Paquette, J.-L., Janots, E., Wirth, R., 2012. Low-temperature alteration of monazite: fluid mediated coupled dissolution–precipitation, irradiation damage, and disturbance of the U-Pb and Th–Pb chronometers. *Chem. Geol.* 330–331, 140–158.
- Stein, H.J., 2014. Dating and tracing the history of ore formation. In: Holland, H.D., Turekian, K.K. (Eds.), *Treatise on Geochemistry*, second ed. Elsevier, Oxford, pp. 87–118 v. 13.
- Stein, H.J., Yang, G., Zimmerman, A., Pandit, M.K., Raut, P.K., Hannah, J.L., 2007. Re-Os dating of arsenopyrite: Panacea of problematic? *Geological Society of America Abstracts with Programs* 39 (6), 276.
- Tuisku, P., Huhma, H., 2006. Evolution of Migmatitic Granulite Complexes: implications from lapland granulite belt, Part II: isotopic dating. *Bull. Geol. Soc. Finland* 78, 143–175.
- Vaasjoki, M., 1981. The lead isotopic composition of some Finnish galenas. *Geological Survey of Finland, Bulletin* 316, 25p.
- Vallini, D., Rasmussen, B., Krapež, B., Fletcher, I.R., McNaughton, N.J., 2002. Obtaining diagenetic ages from metamorphosed sedimentary rocks: U-Pb dating of unusually coarse xenotime cement in phosphatic sandstone. *Geology* 30, 1083–1086.
- Vallini, D., Rasmussen, B., Krapež, B., Fletcher, I.R., McNaughton, N.J., 2005. Microtextures, geochemistry and geochronology of authigenic xenotime: constraining the cementation history of a Palaeoproterozoic metasedimentary sequence. *Sedimentology* 52, 101–122.
- van Achtenberg, E., Ryan, C.G., Jackson, S.E., Griffin, W.L., 2001. Data reduction software for LA-ICP-MS. In: Sylvester, P. (Ed.), *Laser Ablation-ICPMS in the Earth Science*. Mineralogical Association of Canada, pp. 239–243.
- Väänänen, J., Lehtonen, M., 2001. U–Pb isotopic age determinations from the Kolari-Muonio area, western Finnish Lapland. In: Vaasjoki, M. (Ed.), *Radiometric Age Determinations from Finnish Lapland and their Bearing on the Timing of Pre-cambrian Volcano-sedimentary Sequences*. *Geol. Surv. Finland Spec. Pap.* 33, pp. 85–93.
- Vielreicher, N.M., Ridley, J.R., Groves, D.I., 2002. Marymia: an Archean, amphibolite facies hosted, orogenic lode-gold deposit overprinted by Palaeoproterozoic orogenesis and base metal mineralisation, Western Australia. *Miner. Deposita* 37, 737–764.
- Vielreicher, N.M., Groves, D.I., McNaughton, N.J., Fletcher, I.R., 2015. The timing of gold mineralization across the eastern Yilgarn craton using U-Pb geochronology of hydrothermal phosphate minerals. *Miner. Deposita* 50, 391–428.
- Ward, P., Härkönen, I., Nurmi, P.A., Pankka, H.S., 1988. Structural studies in the Lapland greenstone belt, northern Finland and their application to gold mineralization. In: Autio, S. (ed.) *Current Research 1988*. Geological Survey of Finland, Special Paper 10, pp. 71–77.
- Williams, M.L., Jercinovic, M.J., Harlow, D.E., Budzyń, B., Hetherington, C.J., 2001. Resetting monazite ages during fluid-related alteration. *Chem. Geol.* 283, 218–225.
- Wyche, N.L., Eilu, P., Koppström, K., Kortelainen, V., Niiranen, T., Välimaa, J., 2015. The Suurikuusikko Gold Deposit (Kittilä Mine), Northern Finland. In: Maier, W.D., Lahtinen, R., O'Brien, H. (Eds.), *Mineral deposits of Finland*. Elsevier, Amsterdam, pp. 411–433.
- Zartman, R.E., Doe, B.R., 1981. Plumbotectonics – the model. *Tectonophysics* 75, 135–162.
- Zhang, J., Linnen, R., Lin, S., Davis, D., Martin, R., 2014. Paleoproterozoic hydrothermal reactivation in a neoproterozoic orogenic lode-gold deposit of the southern Abitibi subprovince: U-Pb monazite geochronological evidence from the Young-Davidson Mine, Ontario. *Precamb. Res.* 249, 263–272.
- Zhu, X.K., O'Nions, R.K., 1999. Monazite chemical composition: some implications for monazite geochronology. *Contrib. Miner. Petrol.* 137, 351–363.
- Zi, J.-W., Rasmussen, B., Muhling, J.R., Fletcher, I.R., Thorne, A.M., Johnson, S.P., Cutten, H.N., Dunkley, D.J., Korhonen, F.J., 2015. In situ U-Pb geochronology of xenotime and monazite from the Abra polymetallic deposit in the Capricorn Orogen, Australia: dating hydrothermal mineralization and fluid flow in a long-lived crustal structure. *Precamb. Res.* 260, 91–112.